

Numerical Methods for Evading the Sign Problem

A Primer on Complex Langevin and Lefschetz Thimble Methods

Summer Project Report 2021



Department of Physical Sciences
Indian Institute of Science Education and Research
(IISER) Mohali

July 9, 2021

Author: Kunal Verma

Supervisor: Dr. Anosh Joseph

Abstract

Most simulations in Lattice QCD involve the use of algorithms based on Monte Carlo importance sampling. However, more often than not, the probability weights that the method utilizes turn out to be negative, or worse, complex valued. This renders Monte Carlo methods unusable for such problems. In such cases, one says that the theory on the lattice is plagued by the *sign problem*. The most standard example of such a problem is QCD at finite chemical potential. In this report, we will discuss and review two main candidates which might help in evading the sign problem - the complex Langevin method, and the Lefschetz thimble method. The former can be viewed as a complexified generalization of stochastic quantization using the Langevin equation, whereas the latter is a deformation of the original integration contour using the holomorphic gradient flow equation. We will apply these methods to two well-known toy models - the quartic model with a linear term, and the $U(1)$ one-link model with determinant, and compare the results from numerical simulations of the two methods with the exact values, wherever possible.

Acknowledgements

First of all, I would like to express my sincere gratitude to Dr. Anosh Joseph for giving me an opportunity to be a part of this project, and for providing his time and support with multiple meetings throughout the week. On that note, I would also like to thank all of my summer research group members for providing a lot of insight and helping in deepening my understanding of the work.

I would also like to thank the Computer Centre, IISER Mohali, for providing me with remote access to Mathematica, and providing a dedicated system for my work.

I owe my deep gratitude to Roshan Kaundinya for having interesting and insightful discussions with me for hours on end despite his busy schedule, which helped in my fundamental understanding of the Lefschetz thimble method.

I am also indebted to one of my friends who is a PhD student, who would like to remain anonymous, for his immense patience and support, for guiding me through the motivations behind the complex Langevin and Lefschetz thimble methods, spending hours answering my questions, and providing me with relevant resources as well as research papers to learn from.

My special thanks to Dr. Yuya Tanizaki, for having a tremendously productive discussion through email correspondence on the application of the Lefschetz thimble method for finite integration domains by providing plenty of examples and also taking the time to go through my arguments.

Finally, I would like to thank my friends, and most importantly my family, who were always there for me, and for their encouragement and support all through my studies, especially through these difficult times.

Contents

1	Introduction	5
2	Path Integral Approach to Quantum Theory	7
2.1	Analogy with Statistical Mechanics	9
3	Complex Langevin Dynamics	11
3.1	Stochastic Processes	11
3.2	Real Langevin Equation	12
3.2.1	Derivation of the Fokker-Planck Equation	13
3.2.2	Proof for the Long-Time Limit of the Probability Distribution	15
3.3	Complex Langevin Equation	16
3.4	Numerical Simulations of Langevin Dynamics	17
3.4.1	Real Langevin Simulations (With a Toy Problem)	17
3.4.2	Complex Langevin Simulations	20
3.4.3	Quartic Model with a Linear Term	22
3.4.4	$U(1)$ One-Link Model with Determinant	24
4	Lefschetz Thimbles	30
4.1	Saddle Point Method	30
4.1.1	Thimble Decomposition Formula	33
4.2	Lefschetz Thimbles for 0-Dimensional Models	33
4.2.1	Lefschetz Flow Equation	34
4.2.2	Lefschetz Thimble Method: Application to a Toy Problem	37
4.2.3	Quartic Model with a Linear Term	40
4.2.4	$U(1)$ One-Link Model with Determinant	42
5	Conclusion: Thimbles and Langevin Dynamics	47

1 Introduction

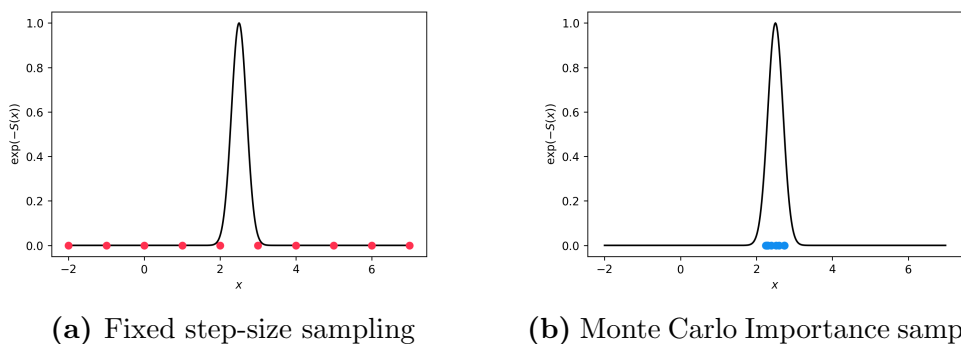
Quantum chromodynamics (QCD) is the quantum field theory of the strong interaction between quarks and gluons, which are the basic degrees of freedom that make up hadronic matter such as protons and neutrons. The QCD Lagrangian, in principle gives the complete description of the theory. However, the equations that it leads to are notoriously hard to solve. Therefore, various techniques have been developed to work with QCD.

Since the perturbative methods are limited in scope, various non-perturbative methods are used by the community, with Lattice QCD being one of the most well established methods. Lattice QCD is formulated on a discrete grid or lattice of points in Euclidean spacetime. In the limit of grid size becoming infinite and site spacing becoming vanishingly small, the continuum QCD is recovered. One of the advantages of transcribing QCD onto a spacetime lattice is that Lattice QCD can be simulated on a computer using methods analogous to those used for Statistical Mechanics (SM), a connection that we will revisit again in a while.

The primary quantities of our interest (just like in SM) are the partition function Z and the expectation values of the observables

$$\langle O(\phi) \rangle = \frac{\int \mathcal{D}\phi O[\phi] e^{-S[\phi]}}{\int \mathcal{D}\phi e^{-S[\phi]}} = \frac{1}{Z} \int \mathcal{D}\phi O[\phi] e^{-S[\phi]}. \quad (1.1)$$

The most acknowledged class of methods used in Lattice QCD simulations is based on Monte Carlo importance sampling. This method interprets the Boltzmann factor e^{-S} (or $e^{-\beta E}$ for SM) as a weight factor, and generates the sampling points according to that weight factor. To demonstrate its strength over standard fixed step-size sampling, we take a simple example of a function which is sharply peaked around a point.



In this example, the fixed step-size sampling simply fails to sample the points where the contribution to the integral would be largest, whereas Monte Carlo importance sampling manages to sample all the points in the region where the function peaks, hence giving a much better approximation to the integral. Thus, Monte Carlo sampling methods, due to their wide applicability and high accuracy are the go-to tool for Lattice QCD practitioners.

However, the story does not end here. Monte Carlo simulations work fine as long as the action $S \in \mathbb{R}$, since e^{-S} remains a positive number. A problem arises when the action $S \in \mathbb{C}$. This typically occurs in QCD when the fermion chemical potential $\mu \neq 0$. In

such cases, S is in general a complex number, so the Boltzmann factor e^{-S} cannot be interpreted as a “probability weight” anymore. This is the so-called **sign problem** or the **complex action problem** in Lattice QCD. This major unsolved problem prevents the use of the lattice methods to predict phases and properties of quark matter.

The simplest idea to overcome the sign problem which still allows the use of MC sampling is the *reweighting procedure*, where the Boltzmann factor is split into real and imaginary parts $e^{-S} = e^{-S_R} e^{-iS_I}$, the imaginary phase e^{-iS_I} is incorporated into the observable, and e^{-S_R} is used as the new weight. But due to the highly oscillatory function in the leftover integrand, using MC importance sampling leads to very small numbers, whose exact value gets swamped by the inherent noise in the MC sampling process.

Nonetheless, there do exist other approaches which aim to solve the sign problem altogether. They are comparatively recent, and still in development, but they do show significant potential in taming the sign problem. This report will focus on two such methods

1. **Complex Langevin method:** Based on stochastic quantization of the fields. The field configuration is evolved according to a SDE and its equilibrium configuration is chosen as the sampling configuration.
2. **Lefschetz Thimble method:** New manifolds, equivalent to the original domain of integration, are found in the complexified space, along which the imaginary part of the action is constant and, therefore, the integral is (mostly) real.

In this report, we will explore both the methods with a variety of toy-models, and compare our results with exact values wherever possible. Since both methods rely on complexifying the fields, it is worth investigating the similarities and differences between the two. We will exclusively be dealing with 0-dimensional QFTs since they serve as an excellent playground of ideas to work on, which can then be generalised to higher dimensions. A **0-dimensional QFT** is exactly like a standard QFT, but with 0 space-time dimensions where it is just a single point $\{\text{pt}\}$, so the field configuration ϕ becomes a simple map $\phi : \{\text{pt}\} \rightarrow \mathbb{R}$, or in other words, just a real variable. In this light, the action functional $S[\phi]$ reduces to a function $S(\phi)$. This allows us to study properties of QFTs without having to work with multiple dimensions.

2 Path Integral Approach to Quantum Theory

In this section, we will briefly review the similarities between the path integral of QFT and its connection to SM when Euclidean time is introduced. In very loose terms, we will see that the quantum degrees of freedom on a *discretized* spacetime can be identified as the ones in the canonical ensemble at inverse temperature β . (Note: This section can be skipped without loss of continuity.)

Let us consider a non-relativistic quantum system ((0 + 1)-D QFT) described by the Hamiltonian $\hat{H}(\hat{p}, \hat{x})$. The time evolution of the wave function can be described using the unitary operation

$$|\psi(t_f)\rangle = \hat{U}(t_f, t_i) |\psi(t_i)\rangle \quad \text{where} \quad \hat{U}(t_f, t_i) = e^{-\frac{i\hat{H}}{\hbar}(t_f - t_i)} \Theta(t_f - t_i). \quad (2.1)$$

In position space representation, the time evolved wave function can be written as

$$\psi(x_f, t_f) = \langle x_f | \psi(t_f) \rangle = \langle x_f | U(t_f, t_i) | \psi(t_i) \rangle = \langle x_f | U(t_f, t_i) \mathbb{1} | \psi(t_i) \rangle. \quad (2.2)$$

If we now insert the resolution of identity $\mathbb{1} = \int dx_i |x_i\rangle \langle x_i|$ into the above expression

$$\psi(x_f, t_f) = \int dx_i \langle x_f | U(t_f, t_i) | x_i \rangle \langle x_i | \psi(t_i) \rangle = \int dx_i K(x_f, t_f; x_i, t_i) \psi(x_i, t_i), \quad (2.3)$$

where $K(x_f, t_f; x_i, t_i) = \langle x_f | e^{-\frac{i\hat{H}}{\hbar}(t_f - t_i)} | x_i \rangle \Theta(t_f - t_i)$ is called the *propagator* of the theory, or more generally, the *Green's function* of the position space Schrödinger equation. This (x_f, x_i) matrix element gives the transition amplitude to go from x_f to x_i in time $t_f - t_i$. However, we still need to arrive at a simplified expression for $K(x_f, t_f; x_i, t_i)$ for equation (2.3) to make any useful predictions about the time evolution for ψ . We will derive an expression for this amplitude in the form of a summation (a functional integral, really) over all possible paths between the initial and final points. In so doing, we derive the path integral from quantum mechanics.

We will start by splicing the time interval into N tiny intervals of size ϵ such that $t_f - t_i = N\epsilon$, and we will set $\hbar = 1$ for the moment. We can then write the propagator as (ignoring the Heaviside step function)

$$K = \langle x_f | \left(e^{-i\hat{H}\epsilon} \right)^N | x_i \rangle = \langle x_f | \underbrace{e^{-i\hat{H}\epsilon} e^{-i\hat{H}\epsilon} \dots e^{-i\hat{H}\epsilon}}_{n \text{ times}} | x_i \rangle. \quad (2.4)$$

If we now insert a complete set of states using the resolution of identity $\mathbb{1} = \int dx_n |x_n\rangle \langle x_n|$ between each exponential ($N - 1$ insertions) we get

$$K = \int dx_{N-1} \dots dx_1 \langle x_f | e^{-i\hat{H}\epsilon} | x_{N-1} \rangle \langle x_{N-1} | e^{-i\hat{H}\epsilon} | x_{N-2} \rangle \dots \langle x_1 | e^{-i\hat{H}\epsilon} | x_i \rangle. \quad (2.5)$$

Relabelling x_f and x_i as $x_f = x_N$ and $x_i = x_0$, we get a compact form

$$K = \int dx_{N-1} \dots dx_1 \prod_{n=0}^{N-1} \langle x_{n+1} | e^{-i\hat{H}\epsilon} | x_n \rangle. \quad (2.6)$$

Now, let us try to simplify the matrix element $\langle x_{n+1} | e^{-i\hat{H}\epsilon} | x_n \rangle$ by again using the resolution of identity $\mathbb{1} = \int dp |p\rangle\langle p|$

$$\mathcal{K}_{n+1,n} = \langle x_{n+1} | e^{-i\hat{H}\epsilon} | x_n \rangle = \int dp \langle x_{n+1} | p \rangle \langle p | e^{-i\hat{H}\epsilon} | x_n \rangle. \quad (2.7)$$

We will now use the Trotter product formula to assert that in the limit $N \rightarrow \infty$ and $\epsilon \rightarrow 0$, the exponential can be decomposed as

$$e^{\epsilon(-i\hat{H})} \equiv e^{\epsilon(-i(\hat{T} + \hat{V}))} = e^{-i\epsilon\hat{T}(\hat{p})} e^{-i\epsilon\hat{V}(\hat{x})} + \mathcal{O}(\epsilon^2) \xrightarrow[0]{\text{in the limit } \epsilon \rightarrow 0} \quad (2.8)$$

Using this, the sub interval matrix element $\mathcal{K}_{n,n+1}$ gets rid of all the operators and replaces them with their eigenvalues

$$\mathcal{K}_{n+1,n} = \int_{-\infty}^{+\infty} \frac{dp}{2\pi} e^{-i\epsilon \left[\frac{p^2}{2m} + V(x_n) - p \left(\frac{x_{n+1} - x_n}{\epsilon} \right) \right]} = \sqrt{\frac{m}{2\pi i\epsilon}} e^{i\epsilon \left[\frac{m}{2} \left(\frac{x_{n+1} - x_n}{\epsilon} \right)^2 - V(x_n) \right]}. \quad (2.9)$$

Substituting this sub interval matrix element into the propagator in equation (2.6), the propagator becomes

$$K = \left(\frac{m}{2\pi i\epsilon} \right)^{N/2} \int dx_{N-1} \dots dx_1 \exp \left(i \sum_{n=0}^{N-1} \epsilon \left[\frac{m}{2} \left(\frac{x_{n+1} - x_n}{\epsilon} \right)^2 - V(x_n) \right] \right). \quad (2.10)$$

In the continuum limit $N \rightarrow \infty$ and $\epsilon \rightarrow 0$, the discrete sum becomes an integral

$$\begin{aligned} \sum_{n=0}^{N-1} \epsilon \left[\frac{m}{2} \left(\frac{x_{n+1} - x_n}{\epsilon} \right)^2 - V(x_n) \right] &\rightarrow \int_{t_i}^{t_f} dt \left[\frac{m}{2} \left(\frac{dx}{dt} \right)^2 - V(x(t)) \right] \\ &= \int_{t_i}^{t_f} dt \mathcal{L}(x, \dot{x}) = S[x(t)]. \end{aligned} \quad (2.11)$$

where $\mathcal{L}(x, \dot{x})$ is the Lagrangian of the theory, and for a classical non-dissipative system, is defined as the difference between the kinetic and potential energy functions. The action $S[x(t)]$ is a functional, which takes in a path $x(t)$, and returns a number $\in \mathbb{R}$, defined by the taking the integral of the Lagrangian \mathcal{L} defined on the Minkowski spacetime.

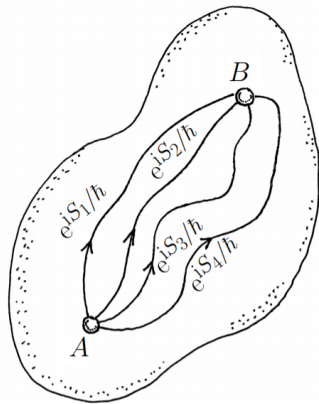


Figure 3: Some possible paths with their amplitudes. A particle will take all of them. (Taken from [26])

Finally, this gives the path integral form of the propagator that we were looking for

$$K = \underbrace{\lim_{\substack{N \rightarrow \infty \\ \epsilon \rightarrow 0}} \left(\frac{m}{2\pi i \epsilon} \right)^{N/2} \int \prod_{n=1}^{N-1} dx_n e^{iS[x(t)]}}_{\int \mathcal{D}[x(t)]} = \int \mathcal{D}[x(t)] e^{iS[x(t)]}. \quad (2.12)$$

The notation $\int \mathcal{D}[x(t)]$ should be taken as a definition of the functional measure over the space of trajectories. Physically, this procedure has the meaning of interpreting the transition probability of a system from a state to another as the sum over all possible paths weighted with the oscillating phase given by their action along each one of them.

2.1 Analogy with Statistical Mechanics

Now let us go back to the analogy with Statistical Mechanics. If we consider a canonical system at inverse temperature β , the partition function of the system can be written as

$$Z(\beta) = \text{Tr}(e^{-\beta H}) = \sum_n e^{-\beta E_n}. \quad (2.13)$$

However, since the trace operation is basis independent, one can rewrite the trace expansion in $|x\rangle$ basis as

$$Z(\beta) = \text{Tr}(e^{-\beta H}) = \int_{-\infty}^{+\infty} \langle x | e^{-\beta H} | x \rangle. \quad (2.14)$$

The similarity with the propagator $K = \langle x_f | e^{-i\hat{H}\Delta t} | x_i \rangle$ is now fairly evident. The last step that we have to take to arrive at the exact analogy between the two is to do a *Wick rotation* into Euclidean time, i.e., $t \rightarrow -i\tau \implies K = \langle x_f | e^{-\hat{H}\Delta\tau} | x_i \rangle$. If we now identify

β with $\Delta\tau$ and restrict ourselves to periodic paths with $x_f = x_i = x$, and sum over all such paths, we get

$$Z(\beta) = \int_{x(0)}^{x(\beta)=x(0)} \mathcal{D}[x(\tau)] e^{-S_E[x(\tau)]} = \mathcal{N} \sum_{\text{sum over all cyclic paths}} e^{-S_E}, \quad (2.15)$$

where

$$S_E = \int_0^\beta d\tau \mathcal{L}_E = \int_0^\beta d\tau \left(\frac{m}{2} \dot{x}^2 + V(x) \right) \quad (2.16)$$

and S_E is called the Euclidean action. This connection between QFT and Statistical Mechanics generalizes to higher dimensions as well. There are close analogies between QFT in d spatial dimensions and Statistical Mechanics in $d+1$ dimensions.

The concept of going into imaginary time also plays a huge role in QFT itself. More often than not, people investigating the properties of QFTs numerically switch to the imaginary time regime, transforming equation (2.12) into the Euclidean path integral

$$Z_{\text{QFT}} = \int \mathcal{D}[x(\tau)] e^{-S_E[x(\tau)]}, \quad (2.17)$$

where we will be loose in calling the QFT path integral as the partition function Z , due to their obvious similarities. Thanks to the Wick rotation, it is now possible to assign every quantum trajectory $x(\tau)$ a *probability weight* based on the action along that path

$$P[x(\tau)] \sim e^{-S_E[x(\tau)]} \quad \text{for } S_E \in \mathbb{R}, \quad (2.18)$$

which is the key to performing Monte Carlo simulations for such models. Nevertheless, since we will be dealing with $(0+0)$ -dimensional QFTs, the partition function simplifies to

$$Z_0 = \int dx e^{-S(x)}. \quad (2.19)$$

3 Complex Langevin Dynamics

There are various ways to quantize a QFT apart from the canonical quantization, with path integrals being one of them. Another alternative method, which was developed by Parisi and Wu [6] in 1980s is known as *stochastic quantization*. In this method, the Euclidean QFT is taken as the equilibrium limit of a system governed by a stochastic process in which the system evolves under a fictitious Langevin time t_L .

In this section, we will review the main concepts behind the Langevin equation, stochastic processes, and how real Langevin dynamics can be used to calculate the partition function Z for real actions. We will then extend the theory for complex actions $S(\phi)$ by complexifying the field such that $\phi \in \mathbb{C}$. We will however, before going into QFT, briefly review the methods of stochastic processes¹ and the mathematical formalism that allows us to model such random behaviour.

3.1 Stochastic Processes

Let us begin with a simple example of a stochastic process, the random jittery movement of a colloid particle suspended in a liquid. This is famously known as the *Brownian motion*, and can be modelled using a stochastic differential equation (for simplicity, we will only deal with the x -direction). Let us say that the particle has a mass m , and the friction coefficient γ , then in the absence of any external potential, the motion of the particle is governed by

$$m\ddot{x} = -\gamma\dot{x} + \eta(t), \quad (3.1)$$

where $\eta(t)$ is the random force that the particle experiences due to all the other atoms in the liquid, and is sometimes referred to as *noise*. The reason why we cannot just integrate this equation like an ordinary differential equation is because we do not actually know what $\eta(t)$ is! We only know some crude features of this noise function, namely

$$\langle \eta(t) \rangle = 0 \quad \langle \eta(t)\eta(t') \rangle = 2D \gamma^2 \delta(t - t'),$$

where the average $\langle \cdot \rangle$ is taken over time. This type of noise is commonly referred to as *white noise* (typically, the noise used has a Gaussian distribution in time domain). The stochastic differential equation (3.1) is known as the *Langevin equation*. We can however, happily integrate the equation (3.1) for a given noise $\eta(t)$ after multiplying by an integrating factor $e^{\gamma t/m}$, and then writing down the integral equation for \dot{x}

$$\begin{aligned} \frac{d}{dt} (\dot{x} e^{\gamma t/m}) &= \frac{1}{m} \eta(t) e^{\gamma t/m} \\ \implies \dot{x}(t) &= \dot{x}(0) e^{-\gamma t/m} + \frac{1}{m} \int_0^t dt' \eta(t') e^{\gamma(t'-t)/m} \end{aligned}$$

¹The section on [Stochastic Processes](#) in David Tong's lecture notes on Kinetic Theory [23] provides a comprehensive review of this topic.

To find the mean velocity, we take averages on both sides, and using the property that averages and integrals commute, we see that

$$\langle \dot{x}(t) \rangle = \dot{x}(0) e^{-\gamma t/m} + \frac{1}{m} \int_0^t dt' \underbrace{\langle \eta(t') \rangle}_{=0} e^{\gamma(t'-t)/m} = \dot{x}(0) e^{-\gamma t/m}. \quad (3.2)$$

Similarly, the expectation values of quadratic functions (which are a bit tedious to calculate) of velocity come out to be

$$\langle \dot{x}(t_1) \cdot \dot{x}(t_2) \rangle = \frac{D\gamma}{m} e^{-\gamma(t_2-t_1)/m} \quad (t_2 \geq t_1 > 0). \quad (3.3)$$

Therefore, specifying the moments of the noise function $\eta(t)$ is enough to calculate all the averages. However, an alternative method is to specify the probability distribution of the noise itself, i.e., the probability that the system acquires the noise $\eta(t)$. Without proof, we claim that the probability distribution that gives *white noise correlations* is given by

$$\text{Prob}[\eta(t)] = \mathcal{N} \exp \left(- \int_{-\infty}^{+\infty} dt \frac{\eta(t)^2}{4D\gamma^2} \right), \quad (3.4)$$

where \mathcal{N} is the normalization factor such that when we “sum” over all the noise functions

$$\int \mathcal{D}\eta(t) \text{Prob}[\eta(t)] = 1. \quad (3.5)$$

3.2 Real Langevin Equation

Since we now have a fair idea about stochastic processes, we will jump straight into the Langevin equation of our interest. We are interested in finding expectation values of the observables $O(\phi)$ where the action is given by $S(\phi)$

$$\langle O(\phi) \rangle = \frac{\int d\phi O(\phi) e^{-S(\phi)}}{\int d\phi e^{-S(\phi)}}. \quad (3.6)$$

Therefore, we desire a method by which we can generate a configuration distributed according to a “probability distribution” $\sim e^{-S}$. A possible algorithm for realizing this is by utilizing the Langevin equation of the form

$$\frac{d\phi(t)}{dt} = - \frac{dS(\phi)}{d\phi} \Big|_{x(t)} + \eta(t), \quad (3.7)$$

where t is the fictitious Langevin time, and $\eta(t)$ is a Gaussian white noise with the following properties

$$\langle \eta(t) \rangle = 0 \quad \langle \eta(t)\eta(t') \rangle = 2\delta(t-t'). \quad (3.8)$$

We present the proof for this, provided that $S(\phi) \in \mathbb{R}$, below.

3.2.1 Derivation of the Fokker-Planck Equation

As discussed in the above subsection, our aim is to give an overview of the proof of the statement that the Langevin equation (3.7) gives rise to the desired equilibrium configuration. We will closely follow the brief but excellent discussion in Ref. [7].

By solving the Langevin equation (3.7), one gets a certain solution $\phi_\eta(t)$ depending on the particular instance of noise $\eta(t)$ that was acquired. For different realizations of the noise $\eta(t)$, we get different solutions and this gives rise to a probability distribution $P(\phi, t)$ which is the probability distribution of the field ϕ , at fictitious time t , and hence this probability distribution changes with time. The average value of an observable can thus be written as

$$\langle O(\phi(t)) \rangle_\eta = \int d\phi P(\phi, t) O(\phi), \quad (3.9)$$

which also changes with time, where the average $\langle \cdot \rangle_\eta$ is over all the realizations of the white noise. We will now derive the time evolution of this probability density $P(\phi, t)$ by taking the derivative with respect to the fictitious time t of both sides of equation (3.9)

$$\frac{d \langle O(\phi(t)) \rangle_\eta}{dt} = \int d\phi O(\phi) \partial_t P(\phi, t). \quad (3.10)$$

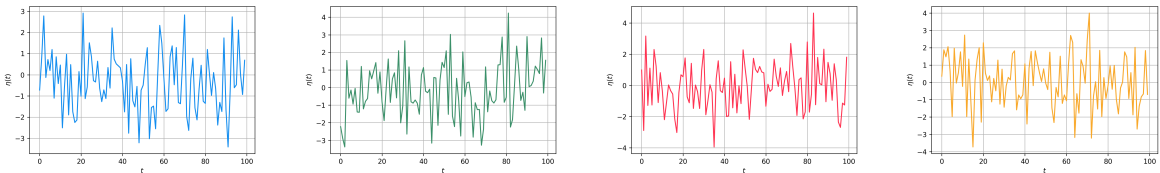


Figure 4: Different realizations of the noise function $\eta(t)$

We now recast equation (3.7) into the form

$$d\phi = -S'(\phi(t))dt + dW(t) \quad \text{where} \quad dW(t) = \int_t^{t+dt} d\tau \eta(\tau). \quad (3.11)$$

We will occasionally use the shorthand notation $S'(\phi(t)) = \left. \frac{dS}{d\phi} \right|_{\phi(t)}$. To evaluate the left hand side of equation (3.10) we will Taylor expand the differential $dO(\phi(t))$ as follows

$$\begin{aligned} O(\phi(t+dt)) &= O(\phi(t)) + \left. \frac{dO}{d\phi} \right|_{\phi(t)} d\phi + \frac{1}{2} \left. \frac{d^2O}{d\phi^2} \right|_{\phi(t)} d\phi^2 + \dots \\ \implies dO(\phi(t)) &= \left. \frac{dO}{d\phi} \right|_{\phi(t)} d\phi + \frac{1}{2} \left. \frac{d^2O}{d\phi^2} \right|_{\phi(t)} d\phi^2 + \dots \end{aligned}$$

On substituting $d\phi$ from (3.11), we can write the differential $dO(\phi(t))$ as

$$\begin{aligned} dO(\phi(t)) &= O'(\phi(t))(-S'(\phi(t))dt + dW(t)) \\ &\quad + \frac{O''(\phi(t))}{2} (dW(t)^2 + S'(\phi(t))^2 dt^2 - 2S'(\phi(t))dt dW(t)). \end{aligned} \quad (3.12)$$

We now note two properties concerning the differential $dW(t)$

$$\begin{aligned}\langle dW(t) \rangle_\eta &= \int_t^{t+dt} d\tau \langle \eta(\tau) \rangle_\eta = 0 \\ \langle dW(t)^2 \rangle_\eta &= \int_t^{t+dt} d\tau \int_t^{t+dt} d\tau' \langle \eta(\tau) \eta(\tau') \rangle_\eta = 2dt.\end{aligned}$$

Now, by taking the expectation value of $dO(\phi(t))$ and only picking the first order terms till dt , we get

$$\begin{aligned}d \langle O(\phi(t)) \rangle_\eta &= dt \langle -S'(\phi(t))O'(\phi(t)) + O''(\phi(t)) \rangle_\eta \\ \implies \frac{d \langle O(\phi(t)) \rangle_\eta}{dt} &= \langle -S'(\phi(t))O'(\phi(t)) + O''(\phi(t)) \rangle_\eta \\ &\stackrel{(3.9)}{=} \int d\phi [-S'(\phi)O'(\phi) + O''(\phi)]P(\phi, t)\end{aligned}$$

Performing integration by parts on the above integral so as to remove the derivatives from $O(\phi)$, we obtain the following expression

$$\begin{aligned}\frac{d \langle O(\phi(t)) \rangle_\eta}{dt} &= \int d\phi O(\phi) [\partial_\phi^2 P(\phi, t) + S''(\phi)P(\phi, t) + S'(\phi)\partial_\phi P(\phi, t)] \\ &\quad + (\text{boundary terms}),\end{aligned}\tag{3.13}$$

where the “boundary terms” are as follows

$$\text{boundary terms} = [O'(\phi)P(\phi, t)O(\phi)\partial_\phi P(\phi, t) - O'(\phi)S'(\phi)P(\phi, t)] \Big|_{\text{boundaries}}.\tag{3.14}$$

Assuming that the boundary terms $\rightarrow 0$ at infinity, and equating (3.10) and (3.13), we obtain the famous Fokker-Planck equation

$$\boxed{\frac{\partial P(\phi, t)}{\partial t} = \frac{\partial}{\partial \phi} \left(\frac{dS}{d\phi} + \frac{\partial}{\partial \phi} \right) P(\phi, t)},\tag{3.15}$$

which can be compactly written as a Schrödinger-like equation by writing a Fokker-Planck Hamiltonian H_{FP}

$$\frac{\partial P(\phi, t)}{\partial t} = -H_{\text{FP}}P(\phi, t) \quad \text{where} \quad H_{\text{FP}} = -\frac{\partial}{\partial \phi} \left(\frac{\partial}{\partial \phi} + \frac{dS}{d\phi} \right).\tag{3.16}$$

Now doing a similarity transformation of the type $\tilde{P}(\phi, t) = e^{S(\phi)/2}P(\phi, t)$, the Fokker-Planck equation transforms to

$$\frac{\partial \tilde{P}(\phi, t)}{\partial t} = -\tilde{H}_{\text{FP}}\tilde{P}(\phi, t),\tag{3.17}$$

where

$$\begin{aligned}
 \tilde{H}_{\text{FP}} &= e^{S(\phi)/2} H_{\text{FP}} e^{-S(\phi)/2} \\
 &= -\frac{\partial^2}{\partial\phi^2} - \frac{S''(\phi)}{2} + \frac{S'(\phi)^2}{4} \\
 &= \left(-\frac{\partial}{\partial\phi} + \frac{S'(\phi)}{2}\right) \left(\frac{\partial}{\partial\phi} + \frac{S'(\phi)}{2}\right).
 \end{aligned} \tag{3.18}$$

3.2.2 Proof for the Long-Time Limit of the Probability Distribution

Since we are assuming $S(\phi)$ to be a \mathbb{R} function here, the operator \tilde{H}_{FP} is a Hermitian operator² because it only admits real inner products over the space of real functions. Also, since we saw that we can decompose \tilde{H}_{FP} as

$$\tilde{H}_{\text{FP}} = \left(-\frac{\partial}{\partial\phi} + \frac{S'(\phi)}{2}\right) \left(\frac{\partial}{\partial\phi} + \frac{S'(\phi)}{2}\right) = B^\dagger B, \tag{3.19}$$

because $(d/d\phi)^\dagger = -d/d\phi$, therefore, we can also conclude that \tilde{H}_{FP} is also positive semi-definite owing to the structure $B^\dagger B$

$$\langle v, \tilde{H}_{\text{FP}} v \rangle = \langle v, B^\dagger B v \rangle = \langle Bv, Bv \rangle = \|Bv\|^2 \geq 0. \tag{3.20}$$

Hence, we can say that \tilde{H}_{FP} is a *Hermitian positive semi-definite operator*, which has a complete set of eigenfunctions $\{p_n(\phi)\}$ with a non-negative spectrum of eigenvalues E_n .

The ground state solution of the eigenvalue equation $\tilde{H}_{\text{FP}} p_n = E_n p_n$ has $E_0 = 0$, with $p_0(\phi) = e^{-S(\phi)/2}$. Now, writing the general solution of the Fokker-Planck equation just as we write the general solution of the Schrödinger equation, we get

$$\tilde{P}(\phi, t) = \sum_{n=0}^{\infty} c_n p_n(\phi) e^{-E_n t} = c_0 e^{-S(\phi)/2} + \sum_{n=1}^{\infty} c_n p_n(\phi) e^{-E_n t}. \tag{3.21}$$

The long time limit of the solution $\tilde{P}(\phi, t)$ as $t \rightarrow \infty$ becomes

$$\lim_{t \rightarrow \infty} \tilde{P}(\phi, t) = c_0 e^{-S(\phi)/2} \implies \boxed{\lim_{t \rightarrow \infty} P(\phi, t) = c_0 e^{-S(\phi)}}. \tag{3.22}$$

This fact together with the ergodic hypothesis makes the Langevin equation (3.7) an excellent tool for producing sets of solutions distributing according to $\exp(-S(\phi))$! However, it is not reasonable to build up the time-dependent probability density $P(\phi, t)$ by solving the Langevin equation for a large number of noise functions $\eta(t)$ and then obtaining the large t limit of that distribution. But we do observe that instead of taking an average over a plethora of noise functions, we can just as well solve the Langevin equation for one noise function over a long time (which is equivalent to a lot of different noise functions generated for small time intervals) and calculate the average over a large

²Given a real function space V , an operator $T \in \mathcal{L}(V)$ is Hermitian iff $\langle Tv, v \rangle \in \mathbb{R} \forall v \in V$.

time interval T after a certain time t_{eq} post which the solutions reach an equilibrium distribution so that

$$\langle O(\phi) \rangle_\eta = \lim_{t \rightarrow \infty} \langle O(\phi(t)) \rangle_\eta \approx \frac{1}{T} \int_{t_{\text{eq}}}^{t_{\text{eq}}+T} d\tau O(\phi_\eta(\tau)) \quad (3.23)$$

The above equation (3.23) is the content of Langevin dynamics simulations.

3.3 Complex Langevin Equation

Now let us discuss the extension of the method for complex actions, i.e., $S(\phi) \in \mathbb{C}$. As soon as we introduce a complex drift term $-S'(\phi)$ into the Langevin equation, we need to extend the domain of the field variable ϕ into the \mathbb{C} plane with $\phi(t) \rightarrow z(t) = x(t) + iy(t)$ and write the Langevin equation as

$$\frac{dz}{dt} = - \left. \frac{dS(z)}{dz} \right|_{z(t)} + \eta(t). \quad (3.24)$$

Note that the noise $\eta(t)$ we use is still \mathbb{R} , for reasons that we will clarify later. To demonstrate that we do not get the same asymptotic behaviour as for the real case, let's introduce an effective “complex valued probability distribution” $P_c(\varphi, t)$ such that

$$\langle O(z(t)) \rangle_\eta = \int d\varphi O(\varphi) P_c(\varphi, t), \quad (3.25)$$

where $\varphi \in \mathbb{R}$ but $P_c(\varphi, t) \in \mathbb{C}$. This complex probability distribution does not really mean anything, but has been introduced just for checking the relaxation dynamics of the complex Langevin equation. Proceeding in the same manner as we did in 3.2.2, we will arrive at the Fokker-Planck equation

$$\frac{\partial \tilde{P}(\varphi, t)}{\partial t} = -\tilde{H}_{\text{FP}} \tilde{P}(\varphi, t) , \quad \tilde{H}_{\text{FP}} = \left(-\frac{\partial}{\partial \varphi} + \frac{S'(\varphi)}{2} \right) \left(\frac{\partial}{\partial \varphi} + \frac{S'(\varphi)}{2} \right).$$

However, we realize that due to the complexity of the action $S(\varphi)$, the arguments for \tilde{H}_{FP} being a Hermitian positive semi-definite operator completely fail, and thus a *general proof of convergence* analogous to (3.22) is not possible for the complex case.

Still, we do not lose hope and proceed to rewrite the Langevin equation using the two independent variables x and y with $z = x + iy$

$$\frac{dx}{dt} = - \text{Re}(S'(z)) + \eta(t) \quad \frac{dy}{dt} = - \text{Im}(S'(z)).$$

We now define a real probability distribution $P(x, y, t)$ being a positive definite function of x and y such that the expectation value of an observable

$$\langle O(z(t)) \rangle_\eta = \int dx dy P(x, y, t) O(x + iy)$$

Again, following the same steps as in the previous subsection 3.2.1, it is straightforward to derive the Fokker-Planck equation for $P(x, y, t)$

$$\frac{\partial P(x, y, t)}{\partial t} = \left(\frac{\partial^2}{\partial x^2} + \frac{\partial \operatorname{Re}(S'(z))}{\partial x} + \frac{\partial \operatorname{Im}(S'(z))}{\partial y} \right) P(x, y, t). \quad (3.26)$$

To obtain the distribution $P(x, y, t)$ by solving the Fokker-Planck equation is however, not straightforward, and has in fact been solved analytically for only a few models. Still, we expect that if the imaginary part of the Fokker-Planck Hamiltonian is sufficiently small, it may still dispense a complete set of eigenfunctions $p_n(x, y)$ with energies E_n . ³

3.4 Numerical Simulations of Langevin Dynamics

As mentioned before, for complex actions $S(z) \in \mathbb{C}$, the Fokker-Planck Hamiltonian is not Hermitian and positive semi-definite anymore. Therefore, in some situations, complex Langevin simulations fail miserably, either giving unstable solutions, or even worse, converging to completely wrong values. However, these problems have been more recently addressed, allowing CLM to become one of the most acknowledged methods when it comes to systems affected by the sign problem.

1. The issue of instabilities was solved by careful integration in the form of taking an adaptive step size ϵ_n approach by keeping the product $\epsilon_n K$ constant, where K is a function of the drift $K = f(\sqrt{\operatorname{Re}(S'(z))^2 + \operatorname{Im}(S'(z))^2})$ to be chosen optimally depending upon the system [16]. This helps reduce the step size along unstable trajectories and allows the real noise $\eta(t)$ to kick the system away from such trajectories. It is for this purpose that including an imaginary component of the noise is counter-productive, and is usually chosen to be $\operatorname{Im}(\eta) = 0$.
2. The issue of convergence of CLM is an issue much more complicated to address. Although there is no definitive solution yet, there has been fundamental progress in that direction, involving *criteria of correctness* where the behaviour of boundary terms is analyzed [17, 18].

We will, however, not bother with these issues for the moment, and state the procedure for numerical simulations starting with a toy example for RLM and then extending the method for CLM.

3.4.1 Real Langevin Simulations (With a Toy Problem)

In order to illustrate the numerical method, we will consider a simple integral as a toy problem with a real action, which has been borrowed from Ref. [20]. In this case, we consider the action

$$S(\phi) = \frac{\mu}{2}\phi^2 + \frac{\lambda}{4!}\phi^4$$

³The interested reader might refer to Viljami Leino's Masters thesis [8], which is an excellent and comprehensive guide on Complex Langevin method, for a detailed discussion of the same.

with real coupling μ and λ . We will keep λ positive, and deal with two separate cases of $\mu > 0$ and $\mu < 0$. The discrete Langevin equation can be written down as

$$\phi_{n+1} = \phi_n - \left(\frac{dS}{d\phi} \right) \Big|_{\phi_n} \Delta t + \eta_n \Delta t. \quad (3.27)$$

However, the innocent looking discrete noise function η_n is not so innocent after all. Let us carefully analyze the discretization procedure for noise now. For the moment, we will generalise the continuous noise function $\eta(t)$ to have a variance Γ

$$\begin{aligned} \langle \eta(t) \eta(t') \rangle &= \Gamma \delta(t - t') & \xrightarrow[\text{continuum}]{\text{discrete}} & \langle \eta_n \eta_m \rangle = c \delta_{nm} \\ \int dt \langle \eta(t) \eta(t') \rangle &= \Gamma & \xrightarrow[\text{continuum}]{\text{discrete}} & \Delta t \sum_{n=1}^{\infty} \langle \eta_n \eta_m \rangle = \Gamma \end{aligned}$$

If we now substitute the value of the $\langle \eta_n \eta_m \rangle$ in the last sum of the above equation, we get

$$\Delta t \sum_{n=1}^{\infty} c \delta_{nm} = \Gamma \implies c = \frac{\Gamma}{\Delta t}.$$

Therefore, the discrete noise correlation for time step n and m can be written as

$$\langle \eta_n \eta_m \rangle = \frac{\Gamma}{\Delta t} \delta_{nm}.$$

To remove the dependence of the variance on Δt , we normalize the variance of the noise to be 1 by redefining the noise as ξ_i such that

$$\eta_n = \sqrt{\frac{\Gamma}{\Delta t}} \xi_n \implies \langle \xi_n \xi_m \rangle = \delta_{nm}.$$

For the ease of recognition of notation, we will switch back to $\xi \rightarrow \eta$ to denote noise, now with unit variance. Thus, we can now rewrite the *discretized* Langevin equation (with $\Gamma = 2$) in its full glory

$$\boxed{\phi_{n+1} = \phi_n - \left(\frac{dS}{d\phi} \right) \Big|_{\phi_n} \Delta t + \sqrt{2 \Delta t} \eta_n} \quad \langle \eta_n \eta_m \rangle = \delta_{nm}. \quad (3.28)$$

As discussed previously, we take the noise η to have a normal distribution in the time domain, now with a variance of 1.

Using the above prescription, the discretized equation for the quartic model can be written down as

$$\phi_{n+1} = \phi_n - \left(\mu \phi_n + \frac{\lambda}{6} \phi_n^3 \right) \Delta t + \sqrt{2 \Delta t} \eta_n.$$

By virtue of the discussion in the previous subsection, we know that in the long-time limit, the samples ϕ_n should follow the probability distribution $P(\phi) \sim e^{-S(\phi)}$. Therefore, after starting out from a randomly produced configuration, we let the sampling process

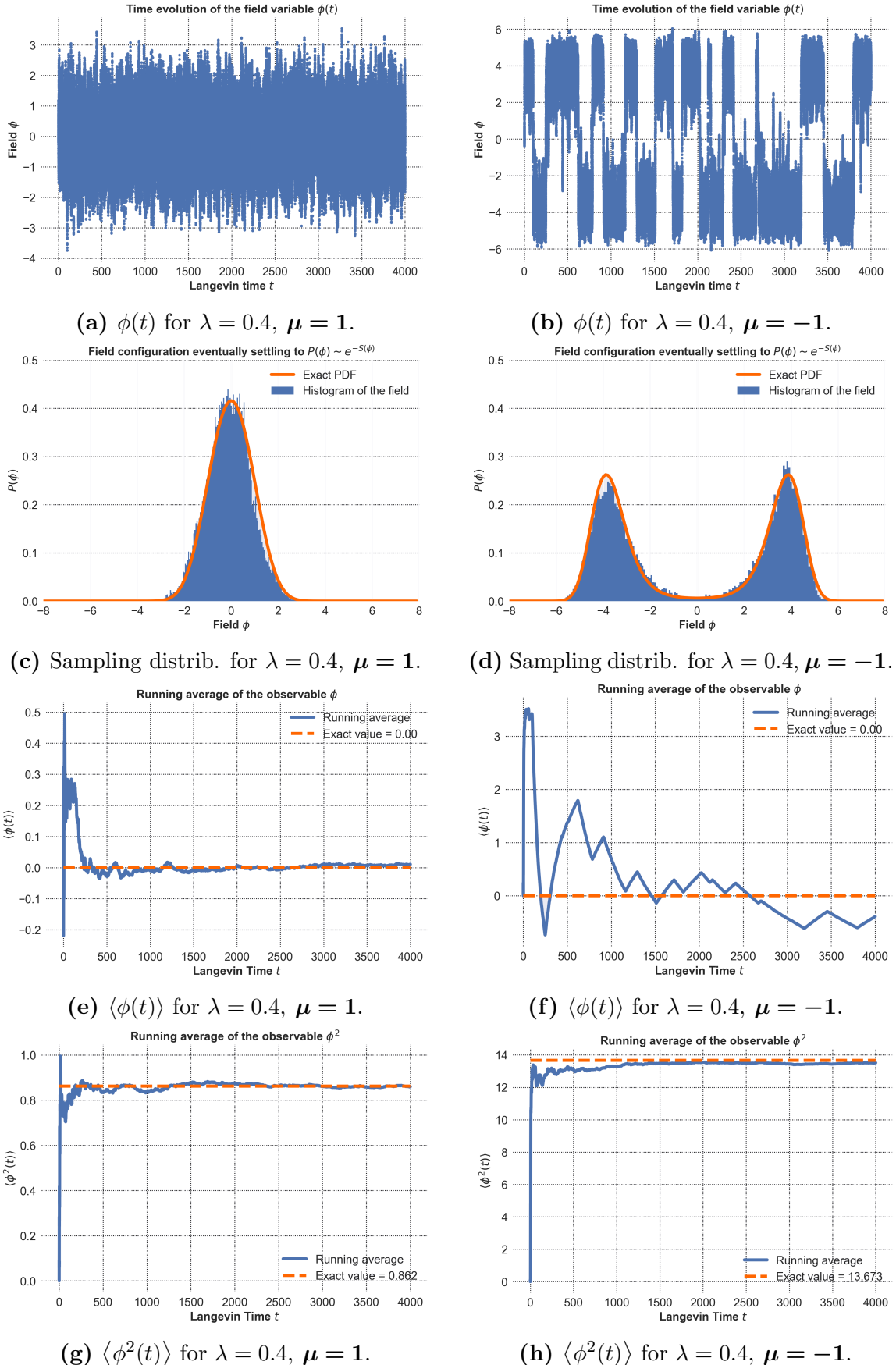


Figure 5: The first row shows the time evolution of the field $\phi(t)$ with Langevin time t . The second row shows that the fields do indeed fall into the distribution $e^{-S(\phi)}$ after thermalisation. The third and the fourth rows show the running averages of $\langle \phi \rangle$ and $\langle \phi^2 \rangle$.

equilibrate for a certain thermalisation time t_{eq} before we start to collect samples.

A detailed analysis of two simulations at fixed $\lambda = 0.4$ and $\mu = \pm 1$ is presented in Fig. 5 (left and right columns respectively). We have plotted the evolution of field configuration $\phi(t)$ (Fig. 5a and Fig. 5b), verified that the samples indeed fall into the distribution $e^{-S(\phi)}$ for $t \rightarrow \infty$ (Fig. 5c and Fig. 5d), and compared the running averages of $\langle \phi \rangle$ (Fig. 5e and Fig. 5f) and $\langle \phi^2 \rangle$ (Fig. 5g and Fig. 5h) with the exact values.

As we can see in the second row of the plots, the histogram of the sampled field values indeed follow the distribution $e^{-S(\phi)}$ in the limit $t \rightarrow \infty$. While in the single-well system $\mu = 1$ (Fig. 5c), this is true to a good approximation, we might often face some issues for the double-well system $\mu = -1$ (Fig. 5d) which suffers from a slight asymmetry. This can occur when the random process gets stuck in one of the wells and is not able to move into the other one causing most of the probability distribution to lie in one of them.

Observable	Exact	Measured	Observable	Exact	Measured
$\langle \phi \rangle$	0.000	0.011	$\langle \phi \rangle$	0.000	-0.390
$\langle \phi^2 \rangle$	0.862	0.859	$\langle \phi^2 \rangle$	13.673	13.516

(a) $\mu = 1$
(b) $\mu = -1$

Table 1: Expectation values $\langle \phi \rangle$ and $\langle \phi^2 \rangle$

One can even see this problem arising in the calculation of the expectation value $\langle \phi \rangle$ in the third row of Fig. 5. For $\mu = 1$ in Fig. 5e, we see white noise centred around the mean 0, while for $\mu = -1$ in Fig. 5f, we observe several correlated plateaus corresponding to the field being stuck in one of the wells, which is reflected in the large statistical uncertainties. For the calculation of $\langle \phi^2 \rangle$ in the last row however, (Fig. 5g and Fig. 5h) due to the symmetry of the problem, the running averages converge to the exact value relatively smoothly for both $\mu = \pm 1$.

3.4.2 Complex Langevin Simulations

Finally, let us now discuss the method for complex Langevin simulations. Complexifying the field variable $\phi(t) \rightarrow z(t) = x(t) + iy(t)$ gives us the Complex Langevin equation, which we restate

$$\frac{dz}{dt} = - \left. \frac{dS}{dz} \right|_{z(t)} + \eta(t),$$

which can be written separately as two coupled equations on expanding $z(t) = x(t) + iy(t)$

$$\dot{x} = - \operatorname{Re} \left(\left. \frac{dS}{dz} \right|_{z(t)} \right) + \eta(t), \quad \dot{y} = - \operatorname{Im} \left(\left. \frac{dS}{dz} \right|_{z(t)} \right).$$

Again, here η is a real noise with variance 2. If we now discretize the equation as in the previous section, the extension to the complex case is trivial and leads to the following

discretized Complex Langevin Equations

$$x_{n+1} = x_n - \operatorname{Re} \left(\frac{dS}{dz} \Big|_{z_n} \right) \Delta t + \sqrt{2\Delta t} \eta_n$$

$$y_{n+1} = y_n - \operatorname{Im} \left(\frac{dS}{dz} \Big|_{z_n} \right) \Delta t$$

where η_n is now a discrete Gaussian white noise function with variance 1. The collected sample of field values after thermalisation give rise to a real probability distribution $P(x, y)$ which is supposed to be the equilibrium solution of the Fokker-Planck equation (3.26). Once this equilibrium distribution has been obtained, the expectation values of the observables $O(z)$ can be calculated as

$$\langle O(z) \rangle_\eta = \lim_{t \rightarrow \infty} \langle O(z(t)) \rangle_\eta = \int dx dy O(x + iy) P(x, y) \approx \frac{1}{N} \sum_{k=0}^N O(x_k + iy_k).$$

We will now use this method in two well-known models, the quartic model with a linear term and the $U(1)$ one-link model, to compute the expectation values of a few observables and try to compare them with exact analytical results. But before that...

A short digression into Linear Stability Analysis ^a

Consider the 2D system of equations of the following form

$$\dot{x} = f(x, y) \quad \dot{y} = g(x, y)$$

and suppose that (x_0, y_0) is a fixed point such that $f(x_0, y_0) = g(x_0, y_0) = 0$. If the first derivatives of f and g are non-vanishing at the fixed point (x_0, y_0) , then we can linearize the system around the fixed point

$$\begin{pmatrix} \dot{x} \\ \dot{y} \end{pmatrix} \simeq \begin{pmatrix} \partial_x f & \partial_y f \\ \partial_x g & \partial_y g \end{pmatrix}_{(x_0, y_0)} \begin{pmatrix} x - x_0 \\ y - y_0 \end{pmatrix} = J(x_0, y_0) \begin{pmatrix} x - x_0 \\ y - y_0 \end{pmatrix}.$$

The advantage of doing this is that we can study the local behaviour of the flow around the fixed point. The eigenvectors \vec{v}_1, \vec{v}_2 of the Jacobian $J(x_0, y_0)$ determine the local direction of trajectories of growth/decay while the eigenvalues λ_1, λ_2 determine the nature of the fixed point and are given by

$$\lambda_1 = \frac{\tau + \sqrt{\tau^2 - 4\Delta}}{2} \quad \lambda_2 = \frac{\tau - \sqrt{\tau^2 - 4\Delta}}{2},$$

where τ, Δ are the trace and determinant of $J(x_0, y_0)$, respectively. The nature of the fixed points, depending on the eigenvalues can be characterized as follows

- $\lambda_1 > 0, \lambda_2 > 0 \implies$ Unstable node
- $\lambda_1 < 0, \lambda_2 < 0 \implies$ Asymptotically stable node

- $\lambda_1 > 0, \lambda_2 < 0$ or $\lambda_1 < 0, \lambda_2 > 0 \implies$ Saddle point
- $\lambda_{1,2} = \lambda \pm i\mu, \lambda > 0 \implies$ Unstable spiral point
- $\lambda_{1,2} = \lambda \pm i\mu, \lambda < 0 \implies$ Asymptotically stable spiral point

^aSteven Strogatz's book on Nonlinear Dynamics and Chaos [24] is an excellent resource to learn about the analysis of non-linear models such as the ones we are discussing.

For classical CLM equations (without the noise term), it can be trivially shown using Cauchy-Riemann conditions that if the action $S(z)$ is holomorphic, then

$$\lambda_{1,2} = -\frac{\partial \operatorname{Re}(S'(z))}{\partial x} \pm i \frac{\partial \operatorname{Re}(S'(z))}{\partial y}. \quad (3.29)$$

Thus, the fixed points in complex Langevin always have either repulsive or attractive spiral flow around them.

3.4.3 Quartic Model with a Linear Term

Let us start by writing down the holomorphic action function of the quartic model [14]

$$S(z) = \frac{\sigma}{2}z^2 + \frac{1}{4}z^4 + hz.$$

We will introduce the complexity in this case through the linear term by setting $h = 1+i$. However, we will keep the quadratic term $\sigma = 1$ for simplicity. The Langevin equation for this model can be written as

$$\dot{z} = -(z^3 + \sigma z + h) + \eta.$$

The fixed points, denoted by z_k , are determined by setting the right hand side equal to zero

$$z^3 + \sigma z + h = 0 \implies z_k = e^{2\pi ik/3}D - e^{-2\pi ik/3}\frac{\sigma}{3D}, \quad k = 0, 1, 2,$$

where

$$D = \left(-\frac{h}{2} + \frac{h}{2}\sqrt{1 + \frac{4\sigma^3}{27h^2}} \right)^{1/3}.$$

For $\sigma = 1$ and $h = 1+i$, as expected, three fixed points are generated. The fixed point $z_0 = -0.799 - i0.359$ gives rise to stable spirals (attractive fixed points), while the fixed points $z_1 = 0.219 + i1.369$ and $z_2 = 0.580 - i1.01$ give rise to unstable spirals (repulsive fixed points) under Langevin flow.

Writing $z = x + iy$, the derivative $\partial_z S$ can be written as follows

$$\partial_z S = (x + x^3 - 3xy^2 + 1) + i(y - y^3 + 3x^2y + 1) \quad (3.30)$$

and the corresponding discretized coupled Langevin equations can be written as follows

$$\begin{aligned}x_{n+1} &= x_n - (x_n + x_n^3 - 3x_n y_n^2 + 1) \Delta t + \sqrt{2\Delta t} \eta_n, \\y_{n+1} &= y_n - (y_n - y_n^3 + 3x_n^2 y_n + 1) \Delta t,\end{aligned}$$

where η_n is a zero-mean and unit variance Gaussian white noise. The simulation parameters we chose were $N = 5 \times 10^6$ and $\Delta t = 0.001$, where N is the number of time steps and Δt is the step size, thus the simulation runs for Langevin time $T = 5000$.

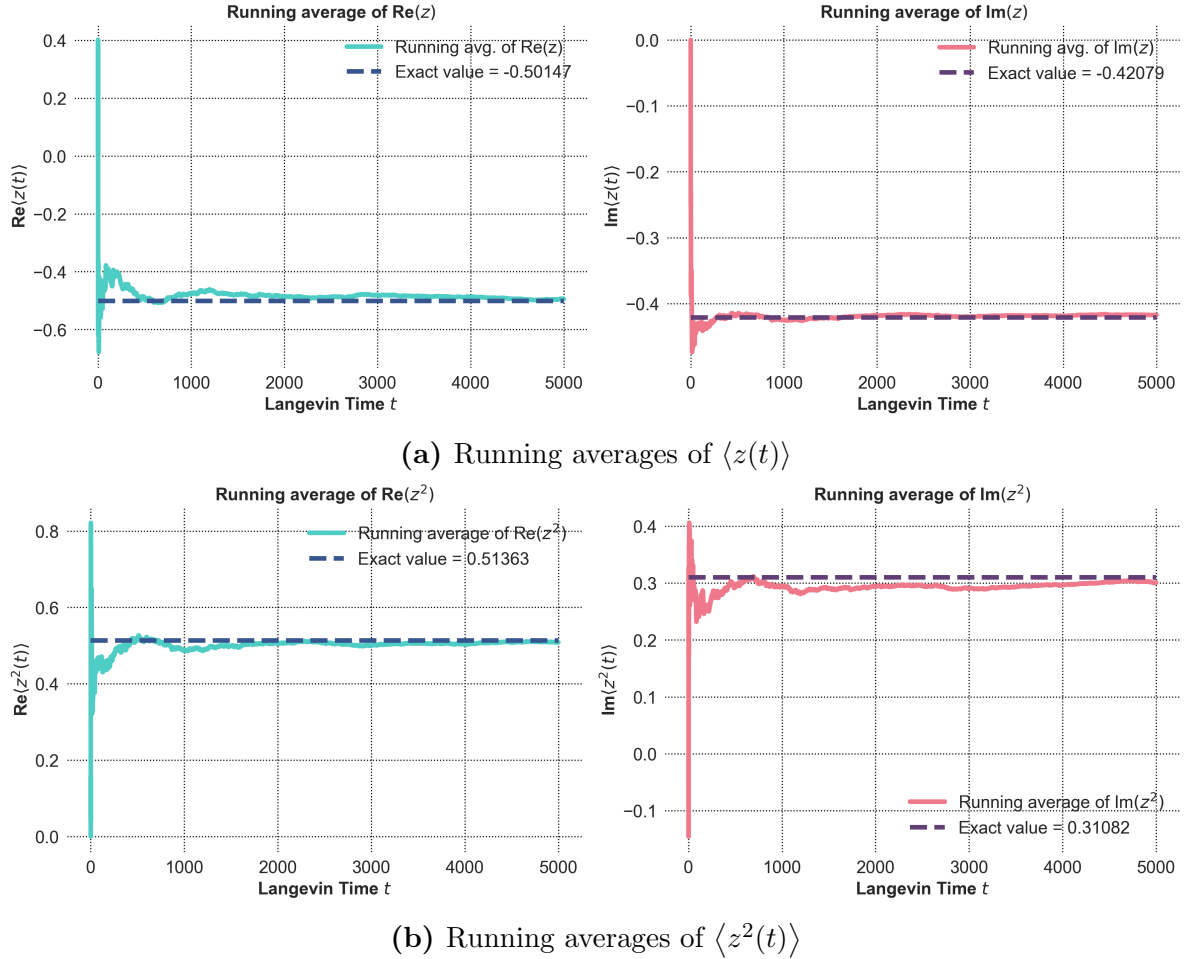


Figure 6

We have plotted the running averages of the expectation values of $\langle z(t) \rangle$ and $\langle z^2(t) \rangle$ in Fig. 6a and Fig. 6b, respectively, i.e., an average of the observable is taken with respect to whatever number of field samples that have been generated till the time step \mathcal{N} . As can be seen in the above, the running averages of the observables converge smoothly to the actual results.

However, we do not consider expectation values such as $\langle z^n(t) \rangle$ where $n > 2$ because the power law decay of the distribution at large distances leads to incorrect convergences. This situation has been discussed in much detail in Ref. [19] where the analysis is done for the same quartic model with $h = 0$ and $\sigma \in \mathbb{C}$, and in fact the analysis carries over immediately to the case discussed here, with $h \in \mathbb{C}$.

Observable	Exact Value	Measured Value
$\langle z \rangle$	$-0.50147 - i0.42079$	$-0.49404 - i0.41732$
$\langle z^2 \rangle$	$0.51363 + i0.31082$	$0.50857 + i0.30071$

Table 2: CLM results for the quartic model with $\sigma = 1$ and $h = 1 + i$.

We have also plotted a heat map of the field distribution $P(x, y)$ generated during the Langevin simulation as a heat map, which is normalized, along with the fixed points z_k and the classical Langevin flow field in Fig. 7. As discussed, the distribution is fairly localised but it decays like a power law at large distances. However, an interesting point to note here is that most of the distribution lies close the attractive fixed point z_0 . An intuitive explanation is as follows: the action function forms a well, with respect to Langevin flow, close to this stable fixed point, and once the field configuration enters this region, it takes a lot of kicks by the noise to make the field leave this region. We will also see the relevance of this distribution in the light of the Lefschetz thimbles later on.

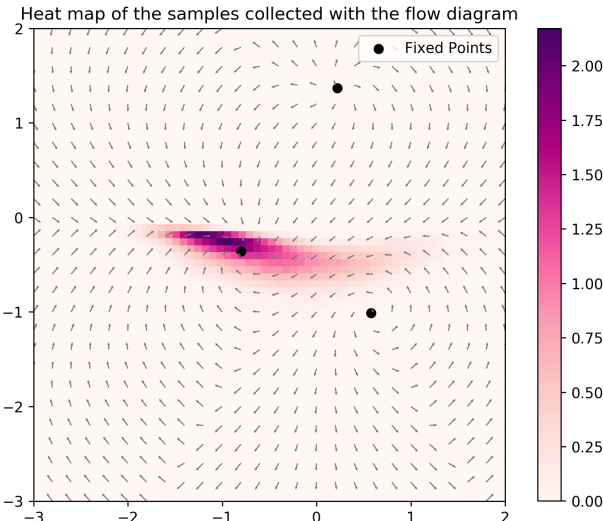


Figure 7: Heat map of the field distribution along from 2D histogram data with the fixed points z_k and the classical Langevin flow vector field.

3.4.4 $U(1)$ One-Link Model with Determinant

The $U(1)$ one-link model is defined in terms of a single degree of freedom x , and the partition function for this model is defined by

$$Z = \frac{1}{2\pi} \int_{-\pi}^{+\pi} dx e^{\beta \cos(x)} (1 + \kappa \cos(x - i\mu)) = \frac{1}{2\pi} \int_{-\pi}^{+\pi} dx e^{-S_{\text{eff}}},$$

where the effective action $S_{\text{eff}} = -\beta \cos(x) - \ln(1 + \kappa \cos(x - i\mu))$. The model has three parameters: β , which appears like an inverse temperature; κ , which appears like a coupling parameter; and μ , which appears like a chemical potential. This toy model is an interesting model to study because it emulates a lattice gauge theory of a single Abelian link variable

e^{ix} with a fermion determinant $\det(M) = 1 + \kappa \cos(x - i\mu)$ that is complex valued due to the presence of a non-zero chemical potential. This leads to a qualitatively new feature, namely a singular drift where determinant vanishes in the complexified plane. Formally, this leads to further breakdown of the justification of complex Langevin dynamics due to lack of holomorphicity and can lead to wrong convergences [12, 13]

For our analysis, just like in Refs. [9, 12, 13], we will consider four observables mimicking the Polyakov loop $\langle U \rangle = \langle e^{ix} \rangle$, the conjugate Polyakov loop $\langle U^{-1} \rangle = \langle e^{-ix} \rangle$, the plaquette $\langle \cos(x) \rangle$ and the density $\langle n \rangle = \partial \ln Z / \partial \mu$. The relevant analytical expressions for the observables and Z are given as follows

$$Z = I_0(\beta) + \kappa I_1(\beta) \cosh(\mu) \quad (3.31)$$

$$\langle U \rangle = \langle e^{ix} \rangle = \frac{1}{Z} [I_1(\beta) + \kappa I'_1(\beta) \cosh(\mu) - \kappa I_1(\beta) \beta^{-1} \sinh(\mu)] \quad (3.32)$$

$$\langle U^{-1} \rangle = \langle e^{-ix} \rangle = \langle e^{ix} \rangle \Big|_{\mu \rightarrow -\mu} \quad (3.33)$$

$$\langle \cos(x) \rangle = \frac{1}{Z} (I_1(\beta) + \kappa I'_1(\beta) \cosh(\mu)) \quad (3.34)$$

$$\langle n \rangle = \left\langle \frac{i\kappa \sin(x - i\mu)}{1 + \kappa \cos(x - i\mu)} \right\rangle = \frac{1}{Z} \kappa I_1(\beta) \sinh(\mu) \quad (3.35)$$

We will use these expressions to compare the numerical simulation results with exact ones. The next step is to complexify the field variable $x(t) \rightarrow z(t) = x(t) + iy(t)$, upon which we get the derivative $\partial_z S$ as

$$\partial_z S = \beta \sin(z) + \frac{\kappa \sin(z - i\mu)}{1 + \kappa \cos(z - i\mu)}.$$

Separating the real and imaginary parts of the derivative gives us the x and y drift terms

$$K_x = \text{Re } \partial_z S(z) = \sin(x) \left(\beta \cosh(y) + \frac{\kappa (\cosh(y - \mu) + \kappa \cos(x))}{D(x, y)} \right),$$

$$K_y = \text{Im } \partial_z S(z) = \beta \cos(x) \sinh(y) + \kappa \sinh(y - \mu) \left(\frac{(\cos(x) + \kappa \cosh(y - \mu))}{D(x, y)} \right),$$

where

$$D(x, y) = (1 + \kappa \cos(x) \cosh(y - \mu))^2 + (\kappa \sin(x) \sinh(y - \mu))^2.$$

Using the above expressions of K_x and K_y , the discretized Langevin equations can be written down as follows

$$x_{n+1} = x_n - K_x \Delta t + \sqrt{2\Delta t} \eta_n,$$

$$y_{n+1} = y_n - K_y \Delta t,$$

where η_n is a zero-mean and unit variance Gaussian white noise. We perform the Langevin simulations by starting from a random initial condition (x_1, y_1) and evaluate the discretized equation in steps to produce a trajectory in the complexified space.

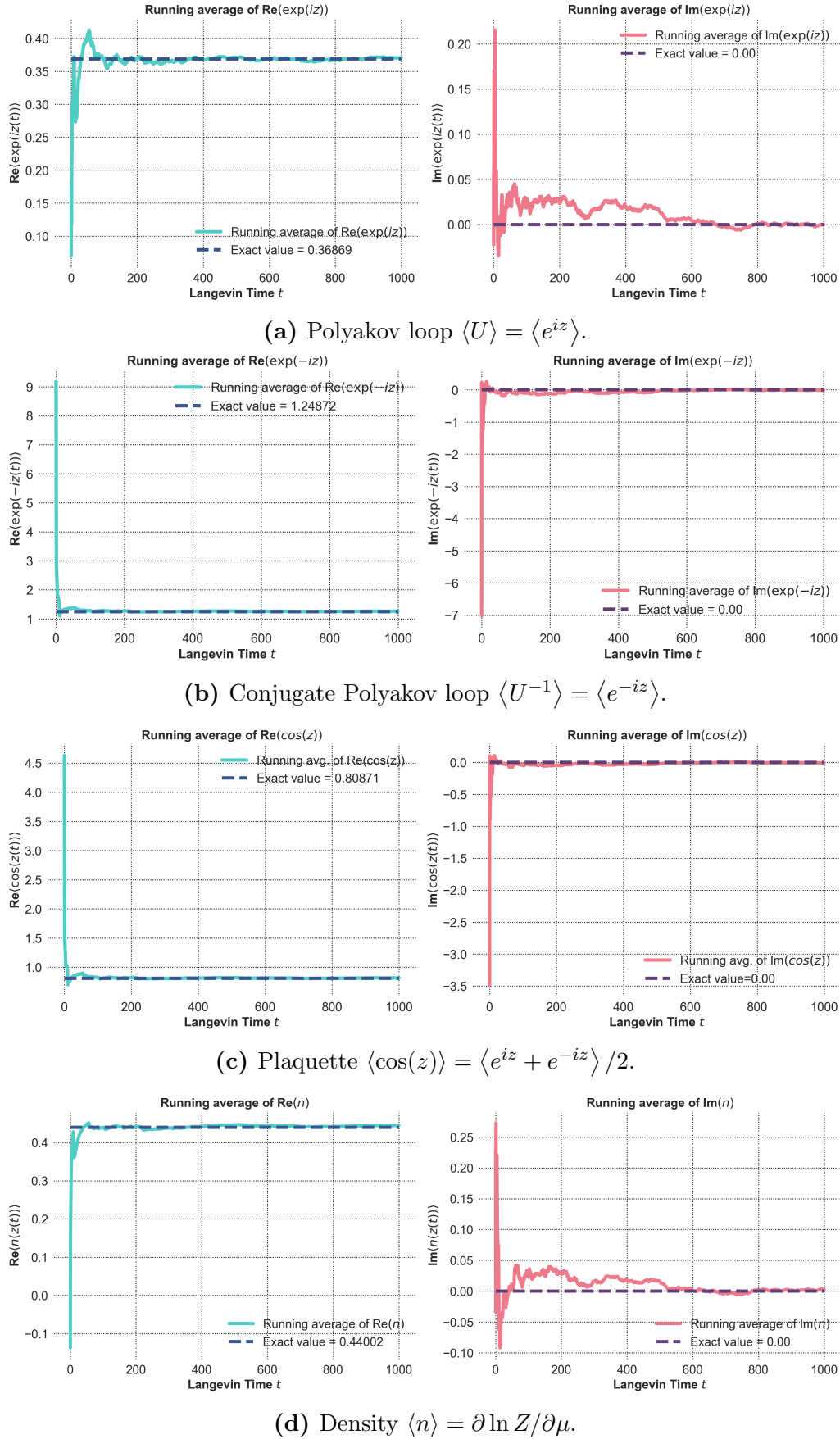
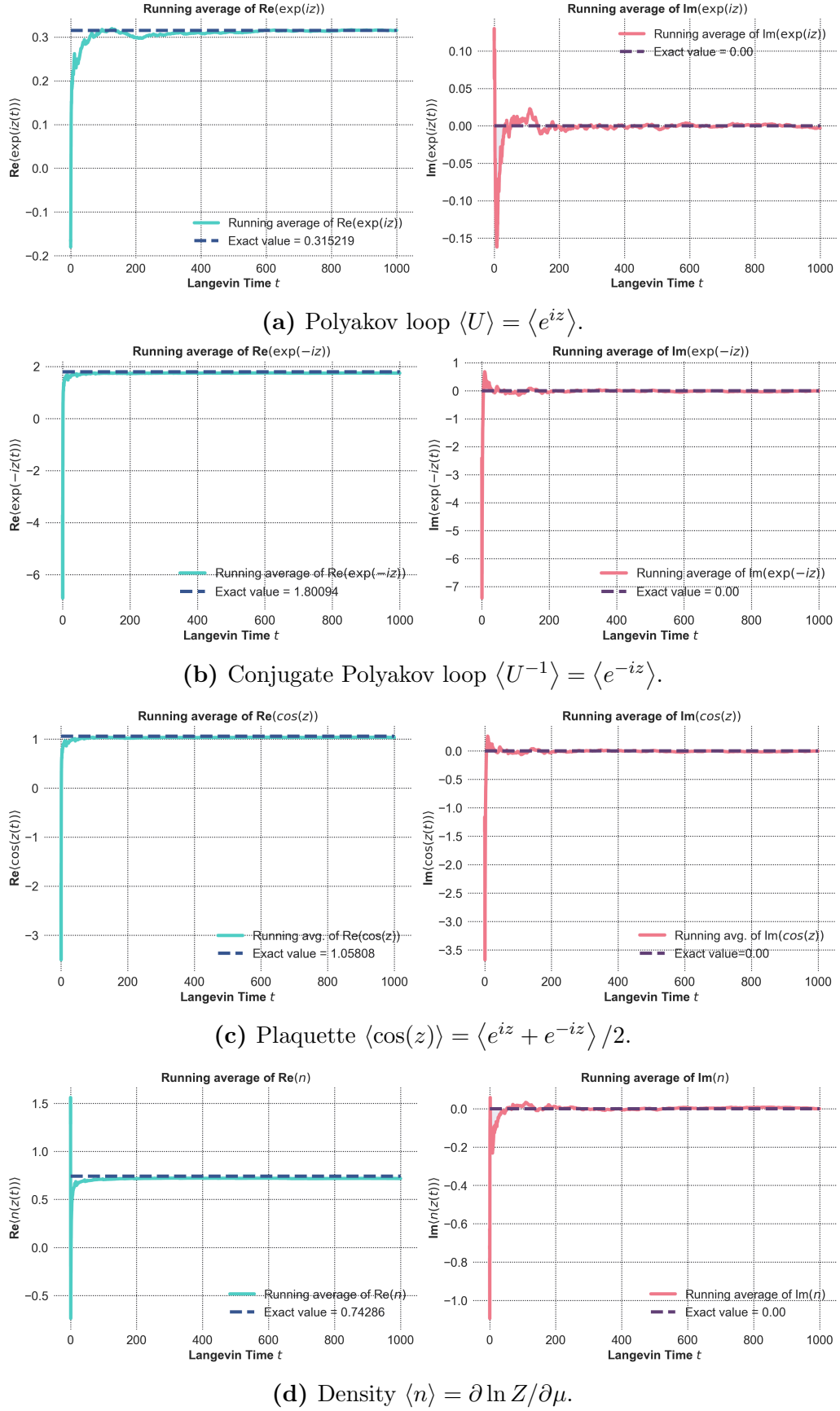


Figure 8: Running averages of the observables for $\kappa = 0.5$.

**Figure 9:** Running averages of the observables for $\kappa = 2.0$.

We perform the simulations for fixed $\beta = 1$ and $\mu = 2$, but two different values of κ , namely $\kappa = 0.5$ and $\kappa = 2$. The simulations were performed for $N = 10^6$ time steps with $\Delta t = 0.001$, resulting in total simulation time $T = 1000$.

In Fig. 8 and 9, we have plotted the running averages of the observables $\langle U \rangle$, $\langle U^{-1} \rangle$, $\langle \cos(z) \rangle$, and $\langle n \rangle$ for $\kappa = 0.5$ and $\kappa = 2.0$, respectively. The calculated expectation values of the observables of interest are indeed close to the exact results for the lowest moments $\langle e^{inz} \rangle$ with small n . However, deviations from the exact analytical results start appearing once the CLM method starts converging to incorrect expectation values for higher moments, which we do not discuss here [12].

Observable	κ	Exact Value	Measured Value
$\langle U \rangle$	$\kappa = 0.5$	0.36869	$0.37073 - i0.00021$
$\langle U^{-1} \rangle$	$\kappa = 0.5$	1.24872	$1.26371 - i0.01567$
$\langle \cos(z) \rangle$	$\kappa = 0.5$	0.80871	$0.81721 - i0.00794$
$\langle n \rangle$	$\kappa = 0.5$	0.44002	$0.44468 + i0.00246$
$\langle U \rangle$	$\kappa = 2.0$	0.31522	$0.31550 - i0.00292$
$\langle U^{-1} \rangle$	$\kappa = 2.0$	1.80094	$1.75123 - i0.00422$
$\langle \cos(z) \rangle$	$\kappa = 2.0$	1.05808	$1.03336 - i0.00357$
$\langle n \rangle$	$\kappa = 2.0$	0.74286	$0.71737 - i0.00011$

Table 3: CLM results for the $U(1)$ model with $\kappa = 0.5, 2.0$.

Lastly, let us look at the heat map of the field distribution $P(x, y)$ for the two cases with $\kappa = 0.5$ and 2.0 , together with the classical flow, and the fixed and singular points.

For $\kappa = 0.5$, the fixed points are found at $z_0 = 0.00 + i0.478$, $z_{1,2} = \pm\pi + i3.387$, $z_{3,4} = \pm\pi + i1.171$ and $z_{5,6} = \pm\pi - i1.036$. The points where the flow $\partial_z S$ is singular are $\tilde{z}_{0,1} = \pm\pi + i0.683$ and $\tilde{z}_{2,3} = \pm\pi + i3.317$.

Similarly, for $\kappa = 2.0$, the fixed points are given by $z_0 = 0.00 + i0.654$, $z_{1,2} = \pm\pi - i0.917$ and $z_{3,4} = \pm2.275 + i2.131$. The singular points of the flow are given by $\tilde{z}_{0,1} = \pm2.094 + i2.00$.

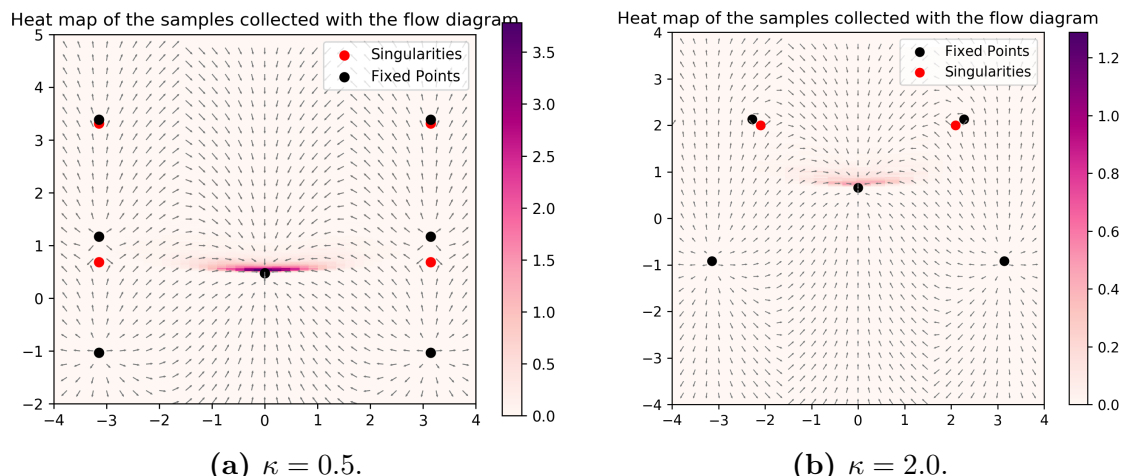


Figure 10: Field distribution heat map, along with the classical Langevin flow, and fixed (black) and singular (red) points.

From Fig. 10, we can roughly see that the distribution is confined close to the center stable fixed point near the origin for $\kappa = 0.5$ (Fig. 10a) and stays away from the poles. We observe a similar pattern for $\kappa = 2.0$ (Fig. 10b), however with much larger excursion to larger y values which makes the distribution much more spread out. The poles are also much closer to the attractive fixed points in this case, and this time CL dynamics manages to reach them. Since the poles are immersed in the distribution, the holomorphicity arguments break down, and even though the simulation results in Table 3 look close enough to actual values, they are not as accurate as for $\kappa = 0.5$ and does not reproduce the correct results at all for higher moments.

We will also explore these models in the light of Lefschetz thimbles in the next section, and we will try to relate the dynamics of the two methods with each other.

4 Lefschetz Thimbles

Very often, we encounter physical systems in QCD, that have a rapidly oscillating action functional $S[\phi]$ (or action function $S(\phi)$ for 0-D), which renders standard numerical integration techniques useless, and makes calculation of expectation values of observables rather difficult. These rapid oscillations of the integrand are a serious problem because we need very high precision to obtain useful results. However, the field of Asymptotic Analysis⁴ in applied mathematics deals with exactly such type of methods by asymptotically evaluating rapidly oscillating integrals [22]. The method that we will discuss in this section goes by the name of the *saddle point method*, which works by complexifying the field ϕ and then using Cauchy's theorem to choose an alternative set of integration contours called *Lefschetz Thimbles* on which evaluation of the integral is a little easier [1, 2].

For the case of higher-dimensional path integrals, the techniques of *Picard-Lefschetz theory* of complex analysis of many variables were proposed to be applied to QFT by Witten [3], which is a higher-dimensional generalisation of the saddle point method. However, we will restrict ourselves again to 0-D QFT and deal with simple one-dimensional integrals⁵.

4.1 Saddle Point Method

Let us start by motivating the need for asymptotic analysis of integrals using an illustration, and try to understand how the saddle point method (also known in literature as the steepest-descent method) tries to evade the sign problem. Consider a complex function $\rho(z) = \text{Re } \rho(z) + i \text{Im } \rho(z)$, and let us say we are interested in evaluating the integral

$$I(\lambda) = \int_{-\infty}^{+\infty} dz f(z) e^{\lambda\rho(z)} \quad \text{where } z \in \mathbb{R}.$$

Now, if the integrand $e^{\lambda\rho(z)}$ is rapidly oscillating along the original cycle \mathbb{R} , then standard numerical integration techniques are hopeless. However, if we now complexify the variable z such that $z \in \mathbb{C}$, we can use Cauchy's theorem (assuming $\rho(z)$ is analytic) and find a contour $\bar{\mathcal{C}}$ on which the integral is easier to evaluate.

As can be seen in Fig. 11, the effect of change of the integration contour by switching from the original cycle \mathbb{R} (red) to the new integration cycle $\bar{\mathcal{C}}$ (blue) can have profound changes on the value of the integrand along that contour. A rapidly oscillating integrand can be converted into a nicely peaked function along the contour $\bar{\mathcal{C}}$, and such a contour integral can be calculated using any standard numerical integration techniques. Therefore, we will now briefly discuss how such new contours are found, and how they can be cleverly utilized in the saddle point method.

⁴Steven Strogatz's lectures on Asymptotic Analysis coupled with the book by Bender and Orszag [25] are good resources to learn about these.

⁵Lorenzo Bongiovanni's PhD Thesis [2] is a fantastic review of different numerical methods used to overcome the sign problem, including Lefschetz Thimbles.

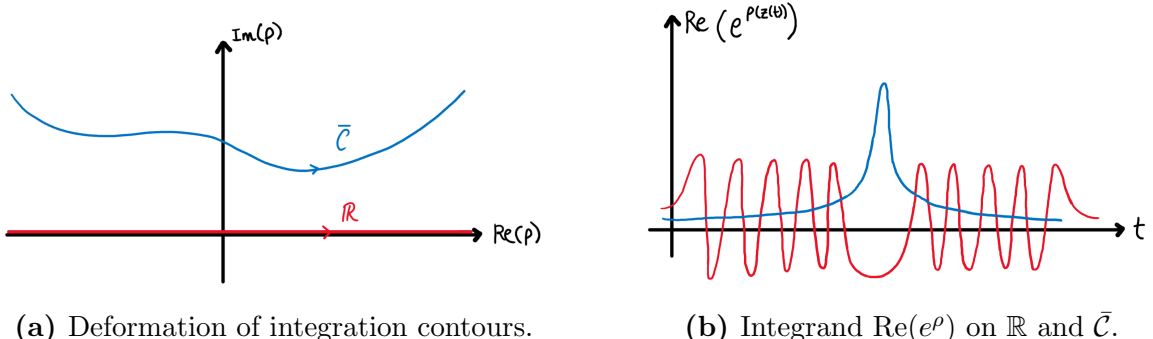


Figure 11: The effect of change of integration cycles. (a) The integration contour \mathbb{R} (red) is deformed into a contour $\bar{\mathcal{C}}$ (blue) which meets it at infinity, thus satisfying Cauchy's theorem. (b) The rapid oscillations of the integrand almost disappear if the integrand $\text{Re}(e^\rho)$ is evaluated along the contour $\bar{\mathcal{C}}$.

Saddle Point Method: The saddle point method originated with Riemann(1892) and is a general technique for finding the asymptotic behaviour of integrals of the form

$$I(\lambda) = \int_{\mathcal{C}} dz f(z) e^{\lambda\rho(z)}$$

as $\lambda \rightarrow \infty$, where $\rho(z) = \phi(z) + i\psi(z)$ with $\phi, \psi \in \mathbb{R}$ and \mathcal{C} is a contour in the complex z -plane. The basic idea is to deform the integral \mathcal{C} to a new contour \mathcal{C}' , using Cauchy's theorem, at least in the domain of analyticity of $f(z)$ and $\rho(z)$. The reason for deforming $\mathcal{C} \rightarrow \mathcal{C}'$ is twofold:

1. We want to deform the path \mathcal{C} so that $\phi = \text{Re } \rho$ drops off either side of its maximum at the fastest possible rate. This path is known as the path of steepest-descent and as $\lambda \rightarrow \infty$, the value of the integral is concentrated around the maxima peak, and can be evaluated using [Laplace's method](#).
2. We want to deform the path \mathcal{C} so that $\psi = \text{Im } \rho$ is constant along it. The purpose of this is to eliminate rapid oscillations in the integrand, and thus we can take out $e^{i\psi(z)}$ out of the integral sign safely.⁶

But the question is, can these seemingly unrelated properties be satisfied together? It turns out that these refer to completely equivalent contours, and we will now prove it.

Proof: Let $\rho(z)$ be an analytic function, and let us restrict ourselves to the domain where $\rho'(z) \neq 0$. We define a *constant-phase contour* of $e^{\lambda\rho(z)}$ where $\lambda > 0$ along which $\psi = \text{Im } \rho$ is constant. We now define a *steepest contour* of $e^{\lambda\rho(z)}$, which is the contour whose tangent is always parallel to $\nabla|e^{\lambda\rho(z)}| = \nabla e^{\lambda\phi(z)}$, which in turn is parallel to $\nabla\phi$.

Since $\rho(z)$ is analytic, it satisfies the Cauchy-Riemann conditions

$$\frac{\partial\phi}{\partial x} = \frac{\partial\psi}{\partial y} \quad \frac{\partial\phi}{\partial y} = -\frac{\partial\psi}{\partial x}$$

⁶We could also deform \mathcal{C} such that $\phi = \text{Re } \rho$ is constant on it, and apply the [method of stationary phase](#). However, Laplace's method is a much better approximation scheme.

which in turn implies that

$$\frac{\partial \psi}{\partial x} \frac{\partial \phi}{\partial x} + \frac{\partial \psi}{\partial y} \frac{\partial \phi}{\partial y} = \nabla \phi \cdot \nabla \psi = 0.$$

Therefore, we can see that $\nabla \psi$ is always perpendicular to $\nabla \phi$. We now recall from the previous paragraph that $\nabla \phi$ is the direction of tangent of the steepest-contour, and since these vectors are in \mathbb{R}^2 , it implies that $\nabla \phi$ is parallel (or anti-parallel) to the curves of constant ψ . So, to summarise, if $\rho(z)$ is analytic with $\rho'(z) \neq 0$, then

Constant-phase contours \equiv Steepest contours

Therefore, we can always deform the integration contour to the one where $\psi = \text{Im } \rho$ is constant, and be assured that the same contour would be the steepest curve for $\phi = \text{Re } \rho$. On this new contour, the asymptotic behaviour of the integral is determined by the behaviour of the integrand near the maxima. These may occur at the end-points, or at an interior point of the constant-phase contour.

If ϕ has an interior maximum at some arbitrary point S on the curve parameterized by s , then we can say that the directional derivative $(\partial \phi / \partial s)_S = 0$. Also, since ψ is constant throughout the curve, $(\partial \psi / \partial s)_S = 0$. Using Cauchy-Riemann conditions, we can further argue and say that $\rho'(z) = 0$ at a point S on the steepest contour where ϕ has an interior maxima. A point where $\rho'(z) = 0$ is called a **saddle point** since the partial derivatives of Re and Im parts of ρ are 0, which leads to saddle points since ϕ and ψ are harmonic functions. However, since $\rho'(z) = 0$ at the interior maximum, the assumption of the above proof breaks down, and results in *two or more steepest-ascent* and *two or more steepest-descent curves* emerging from point S .

Therefore, the saddle point method generates the curves of steepest descent about the saddle points z_k so that we can deform our original integration contour \mathcal{C} into a suitable combination of steepest descent contours on which $\text{Im } \rho = \text{constant}$, at least piecewise, which will evade the sign problem to some extent.

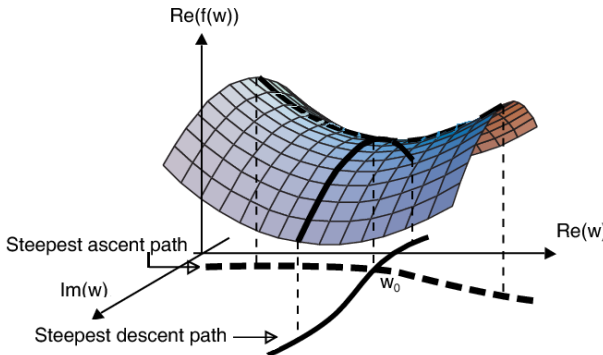


Figure 12: The steepest ascent and descent paths associated to a saddle point w_0 .

4.1.1 Thimble Decomposition Formula

Now that we are aware that we can generate steepest descent curves about the saddle points z_k , we can start thinking of a way to patch together a new contour \mathcal{C}' . But this can be achieved in a number of ways, all of which might not be the most convenient or efficient ones. However, Witten [3] proposed a general way to decompose the original integration cycle in terms of steepest descent and ascent curves. The general result for n -dimensional manifolds is as follows

$$\int_{\mathbb{R}^n} = \sum_m \langle \mathcal{K}_m, \mathbb{R}^n \rangle \int_{\mathcal{J}_m}, \quad (4.1)$$

which is commonly known as the thimble decomposition formula. For $n = 1$, the thimbles \mathcal{J}_m are defined as the steepest descent curves, whereas the anti-thimbles \mathcal{K}_m are defined as the steepest ascent curves. The intersection number $\langle \mathcal{K}_m, \mathbb{R} \rangle = c_m$ denotes the number of intersections the anti-thimble makes with the original integration contour. Each thimble and anti-thimble pair $(\mathcal{J}_m, \mathcal{K}_m)$ is associated to a saddle point z_m and is the only point where they intersect each other.

Therefore, in summary, an integration cycle over the \mathbb{R} interval can be deformed into a sum of integrals over the thimbles \mathcal{J}_m weighted by the intersection number of anti-thimbles \mathcal{K}_m with the original cycle \mathbb{R} , where m is the index of the saddle point z_m with reference to which they are generated. This result is exact, and doing an integral over this new cycle will give exactly the same value of the integral.

4.2 Lefschetz Thimbles for 0-Dimensional Models

Let us now drop all our hesitation and begin working with the integral of our interest, the partition function Z given by

$$Z = \int_{-\infty}^{+\infty} dz e^{-S(z)}$$

with observable expectation values given by

$$\langle O(z) \rangle = \frac{1}{Z} \int_{-\infty}^{+\infty} dz e^{-S(z)} O(z).$$

Here the exponentiated function in the integrand $\rho(z) = -S(z)$. We recall that direct integration is impossible here, and we are interested in deforming the current integration contour \mathbb{R} to a suitable combination of steepest descent contours \mathcal{J} . Thus, we begin by complexifying the variable $z \rightarrow z = x + iy \in \mathbb{C}$, and finding non-degenerate critical points z_m (we will keep switching between the names critical, saddle or fixed points), which are determined by

$$\partial_z S(z) \Big|_{z=z_m} = 0, \quad \partial_z^2 S(z) \Big|_{z=z_m} \neq 0.$$

The thimbles \mathcal{J}_m are then give by the requirement that the $\text{Im } \rho(z) = -\text{Im } S(z)$ remains constant along the thimble, and the resulting steepest descent path for $\rho(z) = -S(z)$ passes through the critical point z_m . Similarly, the anti-thimbles are given by the same requirement that $\text{Im } \rho(z) = -\text{Im } S(z)$ remains constant along the anti-thimble, and the resulting steepest ascent path for $\rho(z) = -S(z)$ passes through the critical point z_m .

The important result is that the observables in the original formulation can now be expressed as

$$\langle O(z) \rangle = \frac{1}{Z} \sum_m c_m e^{-i \text{Im } S(z_m)} \int_{\mathcal{J}_m} dz e^{-\text{Re } S(z)} O(z),$$

where the partition function Z is given by

$$Z = \sum_m c_m e^{-i \text{Im } S(z_m)} \int_{\mathcal{J}_m} dz e^{-\text{Re } S(z)}.$$

The integrals in the above expansions along the thimbles can be calculated by appropriately parameterizing the thimbles, which also introduces the so-called *residual phase*, which comes from the Jacobian due to the curvature of the thimble. To see this for the thimble \mathcal{J}_0 with saddle point z_0 , we will parameterize the thimble as follows

$$\mathcal{J}_0 : \quad x(t) + iy(t), \quad -\infty < t < \infty$$

which results in

$$\int_{\mathcal{J}_0} dz = \int_{-\infty}^{+\infty} dt J(t)$$

where $J(t)$ is the complex Jacobian $J(t) = x'(t) + iy'(t)$, which introduces a residual sign problem. We have thus laid out the general procedure for calculating Z and $\langle O \rangle$ using the Lefschetz thimble method for 0–dimensional models. The generalization to higher dimensions is straightforward.

4.2.1 Lefschetz Flow Equation

Let us recap what we have understood so far. We know that the original integration cycle can be decomposed in terms of Lefschetz thimbles, and we can compute integral over them since the $\text{Im } \rho = \text{constant}$ along these contours, and we know that each of the thimbles is uniquely associated to a saddle point. That is great, but theoretically, how would one proceed towards finding the parameterization of the thimbles and anti-thimbles which are required in the calculation of the integrals (as we saw in the last section)?

For simplicity, we will assume that there exists only one saddle point z_0 for the function $S(z)$. Since both the steepest descent and ascent paths have $\text{Im } \rho(z) = -\text{Im } S(z)$ constant along them, the equation

$$\text{Im } S(z) = \text{Im } S(z_0)$$

should give the thimble and anti-thimble curves associated to the saddle point z_0 . However, this does not give the expression of a parameterized curve, which we will require ultimately to find the integrals. Therefore, we will assume there exists some parameter-

ization $z(t)$ for the thimbles and anti-thimbles, with the constraint that $z(t = 0) = z_0$, giving the parametric equation

$$\text{Im } S(z(t)) = \text{Im } S(z_0) \quad (4.2)$$

In this form, the above equation does not tell us anything. However, if we differentiate this equation, we can find flow equations for this system and use that to generate our desired curves. So, differentiating the above equation (4.2)⁷

$$S(z(t)) - \overline{S(z(t))} = \text{const.} \implies \frac{dS}{dz} \Big|_{z(t)} \frac{dz}{dt} - \overline{\frac{dS}{dz}} \Big|_{z(t)} \overline{\frac{dz}{dt}} = 0.$$

One of the possible flow equations that satisfy the above equation is

$$\boxed{\frac{dz(t)}{dt} = -\overline{\frac{dS}{dz}} \Big|_{z(t)}}. \quad (4.3)$$

This is known in literature as the *Lefschetz flow equation*, which describes the thimbles and anti-thimbles using a flow differential equation. However, it must be emphasized that this is not the only possible flow equation which satisfies $\text{Im}(S(z)) = \text{Im } S(z_0)$. This is just one of the possible equations which describes them. In literature, one can find many different holomorphic gradient flow equations being used, some of them with a plus instead of a minus sign [1], some of them using a normalized flow equation [5], while some of them use a very different flow equation [4] to prevent blow-up while integrating the flow equations. Our task now is to use the Lefschetz flow equation (4.3) to generate the thimble and anti-thimble contours. But before that, let us have a brief interlude on stable and unstable manifolds in dynamical systems.

Stable and unstable manifolds in dynamical systems

We now recall the discussion we had on the nature of fixed points when we linearize a system. One of the possibilities in such a case is that $\lambda_1 > 0$ and $\lambda_2 < 0$ or vice-versa, which gives rise to a **saddle point**. Since one of the eigenvalues is positive and the other is negative, one of the local trajectories (in the direction of eigenvectors) crossing the saddle point denotes exponential decay of the solutions, and the other denotes exponential growth of solutions, hence forming a stable and an unstable manifold.

We can see the stable and unstable manifolds of a critical point, which we assume to be at the point z_0 , in Fig. 13. The arrows show the direction of local flow on the manifolds. The red line denotes trajectories that veer away from z_0 and go

⁷the bar (\bar{S}) here denotes complex conjugation.

out to infinity, and the blue line denotes trajectories that asymptotically approach the point z_0 and stay there forever. Therefore, in forward time, i.e., in the limit $t \rightarrow \infty$, the trajectories are asymptotic to the red line (the unstable manifold), whereas in backward time, i.e., in the limit $t \rightarrow -\infty$, the trajectories are asymptotic to the blue line (the stable manifolds).

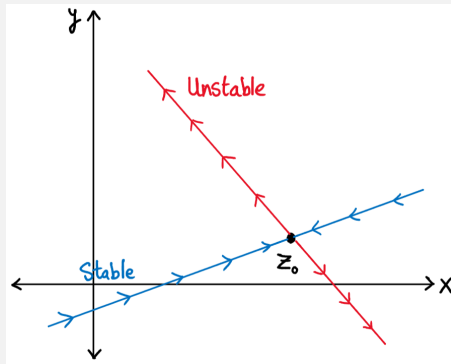


Figure 13: Stable and unstable manifolds of the critical point z_0 .

Mathematically, the **stable manifold** is defined as the set of initial conditions z^* , which asymptotically approach the saddle point $(x(t), y(t)) \rightarrow z_0$ as $t \rightarrow \infty$. Likewise, the **unstable manifold** is defined as the set of initial conditions z^* which asymptotically approach the saddle point $(x(t), y(t)) \rightarrow z_0$ as $t \rightarrow -\infty$.

If we separate the real and imaginary parts of the Lefschetz flow equation, it reduces to a 2-dimensional flow problem, which we can again analyse by methods of non-linear dynamical systems

$$\dot{x} = -\operatorname{Re} \left(\frac{dS}{dz} \right) \Big|_{z(t)} \quad \dot{y} = +\operatorname{Im} \left(\frac{dS}{dz} \right) \Big|_{z(t)}. \quad (4.4)$$

In fact, this is exactly the same as the classical Langevin flow, with the right hand side complex conjugated. Hence, the only change is that all the flow in the y -direction is reflected about the horizontal. Now, let us discuss why we are talking about stable and unstable manifolds in the first place. From the flow equation, we can see that

$$\frac{d(\operatorname{Re} S)}{dt} = \frac{1}{2} \frac{d}{dt} (S + \overline{S}) = \frac{1}{2} \left(\frac{dS}{dz} \frac{dz}{dt} + \overline{\frac{dS}{dz}} \overline{\frac{dz}{dt}} \right) = - \left| \frac{dS}{dz} \right|^2 \leq 0.$$

Therefore, the $\operatorname{Re} S$ monotonically decreases as the parameter value t increases. Now, if we start integrating the system (4.4), starting from $z(t=0) = z_0$

- integrating backwards in time ($t < 0$) generates the initial conditions which reach the critical point z_0 in the limit $t \rightarrow \infty$. (hence, the stable manifold)
- integrating forwards in time ($t > 0$) generates the initial conditions which reach the critical point z_0 in the limit $t \rightarrow -\infty$. (hence, the unstable manifold)

Therefore, we claim that the thimbles and the anti-thimbles are actually nothing but the stable and the unstable manifolds of the flow governed by the system of equations (4.4). This can be proved concretely by observing the following:

- starting from z_0 , integrating forwards generates a curve on which $\text{Re } S$ keeps decreasing (or $\text{Re } \rho$ keeps increasing).
- starting from z_0 , integrating backwards generates a curve on which $\text{Re } S$ keeps increasing (or $\text{Re } \rho$ keeps decreasing).

Recalling the definition of steepest ascent and descent curves, the curves on which $\text{Re } \rho$ drops off either side of z_0 are called steepest descent curves, and the ones on which $\text{Re } \rho$ increases on either side of z_0 are called steepest ascent curves.

Therefore, the $t > 0$ curve forms a part of the steepest ascent curve for $\rho(z)$, and is called the anti-thimble \mathcal{K} , whereas the $t < 0$ curve forms a part of the steepest descent curve for $\rho(z)$ and is called the thimble \mathcal{J} .

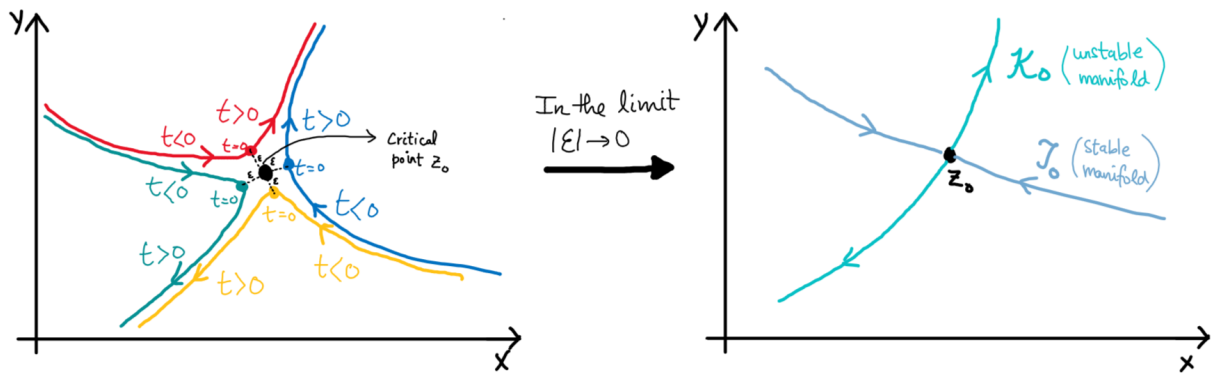


Figure 14: For numerical methods, we generally choose initial conditions very close to z_0 , but in the limit $\epsilon \rightarrow 0$, a combination of all the trajectories gives the entire thimble/anti-thimble structure.

However, if we start integrating the flow equation starting at $z = z_0$, we will just be stuck there since it is a fixed point. Therefore, we start very close to the critical point z_0 , and integrate the flow equation from there because a typical trajectory approaches the unstable manifold as $t \rightarrow \infty$, and the stable manifold as $t \rightarrow -\infty$. However, since the stable/unstable manifolds have a flow coming in/out through two directions, that would only give a part of the thimble/anti-thimble structure as shown in Fig. 14. Thus, we generally integrate the flow equations for two or more points close to the critical point z_0 to get the entire thimble/anti-thimble structure.

In general, all the thimbles (steepest-descent curves) start and end in the regions where $\text{Re } S > 0$, which is a self-consistency check since the integral over $f(z)e^{-S(z)}$ would blow up when integrated along with the thimble if the condition is not satisfied. Hence, $\text{Re } S > 0$ marks what is known as the *region of convergence*.

4.2.2 Lefschetz Thimble Method: Application to a Toy Problem

Let us briefly review the algorithm for finding an integral using the thimble procedure [15]. The partition function Z integral in terms of action $S(z)$ can be written as

$$Z = \int_{-\infty}^{+\infty} dz e^{-S(z)}.$$

The action $S(z) \in \mathbb{C}$, in general, is a rapidly oscillating function, and we try to deform the current integration contour $(-\infty, +\infty)$ into \mathcal{C}' so as to transform the oscillatory integrand into something that is easier to compute. The Lefschetz thimble method suggests that we can equivalently compute the integral as a weighted sum of integral along the thimbles. The equality is exact.

$$Z = \int_{-\infty}^{+\infty} dz e^{-S(z)} = \sum_m \langle \mathcal{K}_m, \mathbb{R} \rangle e^{-i \operatorname{Im} S(z_m)} \int_{\mathcal{J}_m} dz e^{-\operatorname{Re} S(z)}$$

where as always, \mathcal{J}_m and \mathcal{K}_m are the thimbles and anti-thimbles associated to the critical point z_m , respectively. We obtain the thimbles and anti-thimbles by integrating the Lefschetz flow equation

$$\frac{dz(t)}{dt} = -\overline{\frac{dS}{dz}}|_{z(t)}$$

around the critical points z_m . The non-degenerate critical points z_m are obtained by solving for $\partial_z S(z) = 0$, provided that $\partial_z^2 S(z_m) \neq 0$. Another interesting property of the Lefschetz flow equation is that if we linearize the system around the critical points z_m , then using Cauchy-Riemann conditions, it can be shown that the eigenvalues are

$$\lambda_{1,2} = \pm \left| \vec{\nabla} \operatorname{Re} S'(z) \right|.$$

Therefore, the critical/fixed points in Lefschetz flow are *always* saddle points. This is in contrast to Langevin flow where the fixed points always have either a repulsive or attractive spiral flow around them.

Let us now apply the Lefschetz thimble method by starting with a toy example where the integration range is finite, as compared to the infinite integration ranges we usually deal with. Consider the integral

$$I(\lambda) = \int_0^{2\pi} dz e^{i\lambda \sin(z)},$$

where we can think of the effective action as $S(z) = -i\lambda \sin(z)$. However, before proceeding, we pause and analyze if the thimble decomposition formula (4.1) is well-defined for finite integration contours.⁸ It turns out that Lefschetz thimble method works perfectly if the integrand is periodic and the measure of the integration domain is equal to the period, which is 2π for this problem.

An explanation is as follows. Although for infinite integration domains, the thimbles eventually meet the original integration contour at the infinity of the complex plane, for finite integration domains that is not always true. Therefore, for Cauchy's theorem to hold, the steepest descent cycles must be connected to the finite domain endpoints. However, if the integrand is periodic and so is the integration domain, then we can attach the extra contours going to and coming from infinities provided the thimbles start and

⁸Special thanks to Dr. Yuya Tanizaki without whose immense help I would not have figured this out!

end in the region of convergence. Interestingly, the integration along the extra paths cancels out each other due to the periodicity, so it does not change the result. Hence, for the integral $I(\lambda)$ stated above, the LTM is perfectly applicable since the period of the integrand is 2π , and the integration domain is $[0, 2\pi]$. Hence, periodicity is satisfied.

Moving on to finding the thimbles, integrating the flow equation is one of the most simple and straightforward methods to do so. There do exist more sophisticated techniques, some of which are the *axis scan* method [5], the *thimble cooling* method [5, 10], and even analytical methods to find parameterisation of thimbles [11]. However, in this report, we will stick to the direct method of integrating the flow equation.

To construct the thimbles, we start by finding the critical points, determined by

$$\partial_z S = -i\lambda \cos(z) = 0, \quad \partial_z^2 S = i\lambda \sin(z) \neq 0.$$

There are two solutions: $z_0 = \pi/2$ and $z_1 = 3\pi/2$, which belong to the domain $[0, 2\pi]$. We can then integrate the coupled flow equation (4.4) starting close to the critical points such that $z(t=0) \approx z_{0,1}$ to obtain the thimbles and anti-thimbles. The flow equation for this particular instance is

$$\dot{x} = \lambda \sin(x) \sinh(y), \quad \dot{y} = -\lambda \cos(x) \cosh(y).$$

Fig. 15 on the next page shows the thimble structure for the given action. Every fixed point has an associated thimble (the blue line) and an anti-thimble (the red dashed line). We note that the thimbles end asymptotically in the region where the integral converges ($\text{Re } S > 0$) which is shaded in light blue. The intersection number c_m for both the thimbles is 1 since both the anti-thimbles intersect the \mathbb{R} axis exactly once, which implies that $c_{0,1} = \langle \mathcal{K}_{0,1}, \mathbb{R} \rangle = 1$. Therefore, both the thimbles have the same weight in the contribution to the integral.

To verify the finite integration domain argument, we can see that if we introduce two extra contours: one going from the origin at $(0 + i0)$ to $(0 + i\infty)$, and another going from $(2\pi + i\infty)$ down to $(2\pi + i0)$, then these contours combined with the thimbles are clearly a deformation of the original integration domain $[0, 2\pi]$. However, we need not consider these two extra contours since $S(z)$ is analytic and periodic with interval 2π , which causes the integral along these two contours to cancel out. Thus, calculating the integral along the thimbles is sufficient.

All the numerics here are done in Mathematica. We first find a suitable parameterization for the thimbles and then use it to find the integral $I(\lambda)$. The real and imaginary parts of the action can be written as follows

$$\text{Re } S = \lambda \cos(x) \sinh(y), \quad \text{Im } S = -\lambda \sin(x) \cosh(y).$$

Thus, the integral $I(\lambda)$ can be computed as follows

$$I(\lambda) = e^{i\lambda} \int_{\mathcal{J}_0} (dx + idy) e^{-\lambda \cos(x) \sinh(y)} + e^{-i\lambda} \int_{\mathcal{J}_1} (dx + idy) e^{-\lambda \cos(x) \sinh(y)}.$$

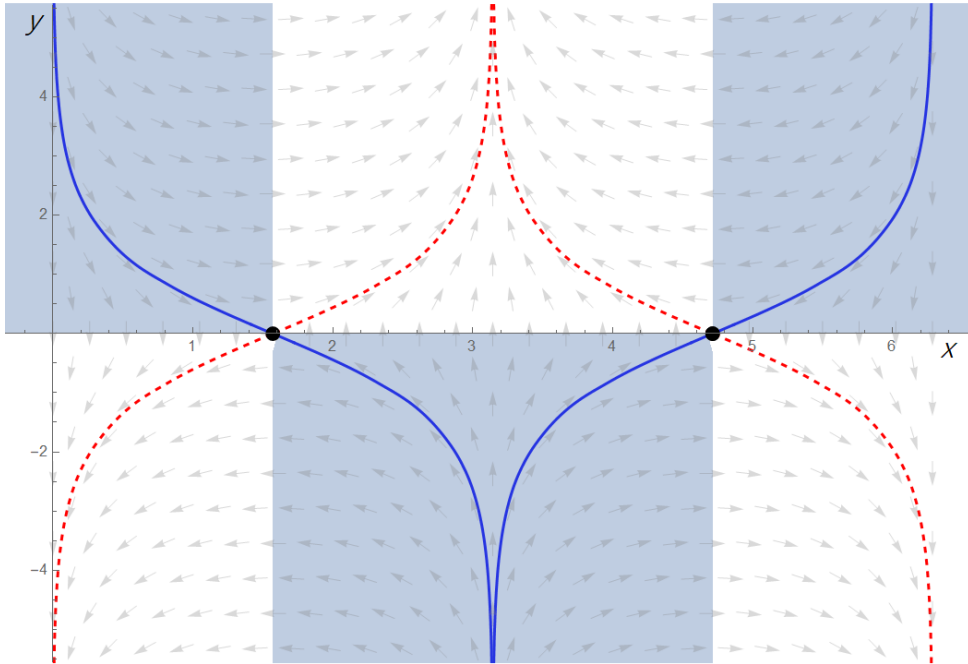


Figure 15: Thimble structure and the Lefschetz flow field for the toy problem with $S(z) = -i\lambda \sin(z)$: the black circles denote the fixed points, the (normalised) arrows the Lefschetz flow, with the blue lines indicating thimbles and red dashed lines indicating anti-thimbles. The light blue regions correspond to the region of convergence $\text{Re } S > 0$.

We have evaluated the integral for the case of $\lambda = 1$, for which the results are shown in the table below. The numerical integration along the thimble is done in an interval which nicely encloses the region where the $-\text{Re}(S)$ peaks, so as to get a nice approximation.

Function	Exact Value	Measured Value
$I(\lambda = 1)$	$1.530 + i 0$	$1.523 + i 2.36 \times 10^{-15}$

Table 4: Comparison of exact and numerical results of the integral.

As can be seen, the numerical result matches very closely with the exact result. We can also see that the imaginary part from both the integrals effectively cancel out, and the difference is only of the order of 10^{-15} which appears due to the lack of precision up to such low orders of magnitudes.

4.2.3 Quartic Model with a Linear Term

Let us now begin the study of the two problems that we discussed in the complex Langevin section as well: the quartic model with a linear term, and the $U(1)$ one-link model with determinant.

Let us begin with the quartic model [14] by writing down the action

$$S(z) = \frac{\sigma}{2} z^2 + \frac{1}{4} z^4 + hz,$$

where we will use the same parameter values $h = 1 + i$ and $\sigma = 1$. The Lefschetz flow equation for the model can be written down as

$$\dot{x} = x^3 - 3xy^2 + x + 1, \quad \dot{y} = y^3 - 3x^2y - y - 1.$$

The fixed points are determined by solving for the equation $\partial_z S = 0$, which for the given parameter values becomes

$$z^3 + z + (1 + i) = 0.$$

This gives the three fixed points as $z_0 = -0.799 - i0.359$, $z_1 = 0.219 + i1.369$ and $z_2 = 0.580 - i1.01$. Associated to each fixed point is a thimble \mathcal{J}_m and anti-thimble \mathcal{K}_m . The thimble structure, along with a 3D plot on the $\text{Re } S$ manifold is shown in the figure below.

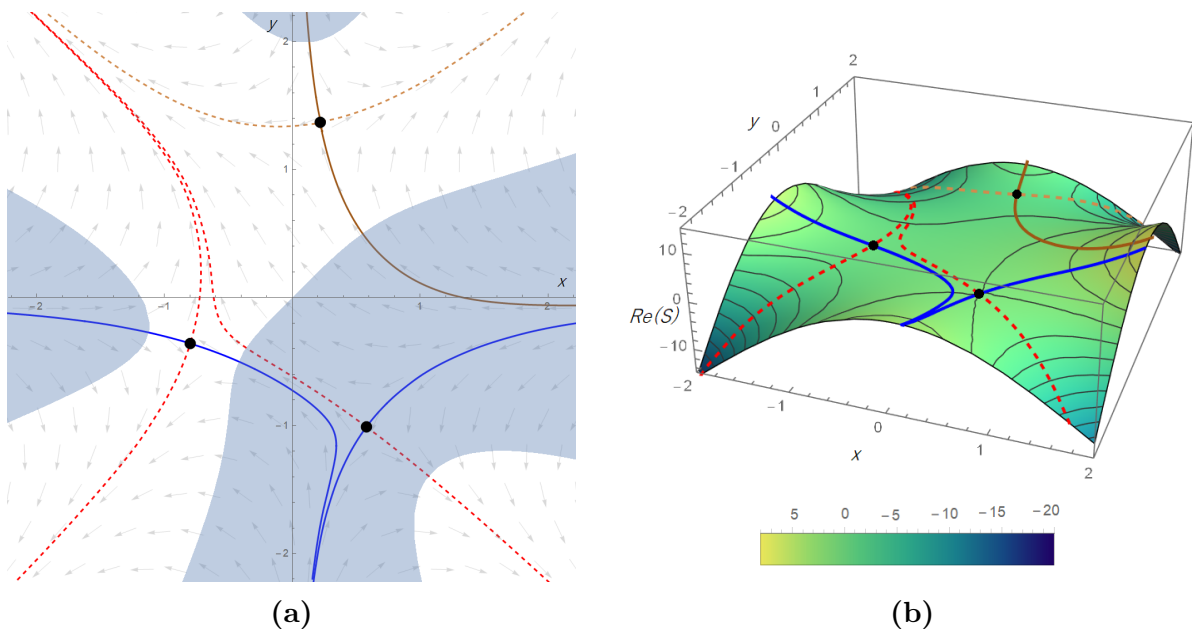


Figure 16: Thimble structure with the Lefschetz flow for the quartic model **(a)** the black circles denote the fixed points $z_{0,1,2}$ with blue (full) lines indicating thimbles and red (dashed) lines anti-thimbles, which contribute to the integral Z . The brown (full) and light-brown (dashed) pair of contours does not contribute since the anti-thimble does not intersect with the \mathbb{R} line. **(b)** the thimble structure is shown on the manifold of $\text{Re}(S)$.

As can be seen from the thimble structure of Fig. 16, the contributing thimbles (in blue) corresponding to the fixed points z_0 and z_2 always lie in the region of convergence $\text{Re } S > 0$ (light blue region). The thimble corresponding to the fixed point z_1 does not contribute to the partition function since the intersection number $c_1 = 0$ as a result of lack of intersection of the anti-thimble \mathcal{K}_1 with the original integration contour \mathbb{R} .

To calculate the integral, we will integrate the flow equation for $t < 0$ and $t > 0$ to obtain the thimble and anti-thimble contours, respectively. Having obtained the contours, we will then use the thimble decomposition to find the partition function Z . The real and

imaginary part of the action can be written as

$$\begin{aligned}\operatorname{Re} S &= \frac{1}{4}(4x + x^4 + 2x^2(1 - 3y^2) + y(y^3 - 2y - 4)) \\ \operatorname{Im} S &= y + x^3y + x(1 + y - y^3)\end{aligned}$$

Thus, the partition function can be written as

$$Z = e^{-i\operatorname{Im} S(z_0)} \int_{\mathcal{J}_0} dz e^{-\operatorname{Re} S(z)} + e^{-i\operatorname{Im} S(z_2)} \int_{\mathcal{J}_2} dz e^{-\operatorname{Re} S(z)}.$$

It is important to parameterize the thimbles \mathcal{J} in a manner such that for the combination of thimbles, the composed direction of parameterization should roughly move from left to right, i.e., in the direction of going from $-\infty$ towards $+\infty$. Similarly, the observable expectation values can be written as

$$\langle O(z) \rangle = \frac{1}{Z} \left[e^{-i\operatorname{Im} S(z_0)} \int_{\mathcal{J}_0} dz e^{-\operatorname{Re} S(z)} O(z) + e^{-i\operatorname{Im} S(z_2)} \int_{\mathcal{J}_2} dz e^{-\operatorname{Re} S(z)} O(z) \right].$$

The results for the calculations of the partition function Z , and the expectation values of $\langle z \rangle$ and $\langle z^2 \rangle$ are summarised in the table below.

Obs.	Exact Value	Contrib. from \mathcal{J}_0	Contrib. from \mathcal{J}_2	Measured Value
Z	$1.76537 + i0.88721$	$1.72754 + i0.47856$	$0.02252 + i0.42420$	$1.75006 + i0.90277$
$\langle z \rangle$	$-0.50147 - i0.42079$	$-0.78656 - i0.44283$	$0.28454 + i0.01724$	$-0.50203 - i0.42559$
$\langle z^2 \rangle$	$0.51363 + i0.31082$	$0.31377 + i0.59323$	$0.19067 - i0.28694$	$0.50444 + i0.30630$

Table 5: Calculation of Z , $\langle z \rangle$ and $\langle z^2 \rangle$ for the quartic model using Lefschetz thimbles.

If we refer back to the analysis of this model using Complex Langevin in section 3.4.3, we notice that both an attractive and a repulsive fixed point under Langevin dynamics contribute to the thimble contour. As can be seen from the contribution of numerical values in the above Table 5 towards the integral, the thimble \mathcal{J}_0 always has a higher contribution, which interestingly corresponds to the thimble associated with the fixed point z_0 which has an attractive fixed point under Langevin dynamics. Hence, the distribution pattern from Langevin dynamics (see Fig. 7) matches very closely with the contribution of the thimbles.

4.2.4 $U(1)$ One-Link Model with Determinant

Finally, let us deal with the $U(1)$ one-link model, now using the Lefschetz thimble method. Recalling from the previous section in complex Langevin dynamics, the partition function of the $U(1)$ model is given by

$$Z = \frac{1}{2\pi} \int_{-\pi}^{+\pi} dz e^{\beta \cos(z)} (1 + \kappa \cos(x - i\mu)) = \frac{1}{2\pi} \int_{-\pi}^{+\pi} dz e^{-S_{\text{eff}}},$$

where the effective action $S_{\text{eff}}(z) = -\beta \cos(z) - \ln(1 + \kappa \cos(z - i\mu))$. The presence of a non-zero chemical potential leads to a complex fermion determinant, and thus, we can

already notice a sign problem for $\kappa > 1$. Furthermore, the action we are left with is not holomorphic anymore, which is reflected in the drift having poles where the determinant $1 + \kappa \cos(z - i\mu)$ is zero

$$\frac{dS}{dz} = \beta \sin(z) + \frac{\kappa \sin(z - i\mu)}{1 + \kappa \cos(z - i\mu)}.$$

For the case of thimbles, the violation of holomorphicity can compromise the deformation of original contour of integration. However, as we shall see, the thimbles usually end on the poles, so the integrals over thimbles are not affected by it. Nevertheless, this is an important problem to deal with, since the action of the theory is usually non-holomorphic in the case of full QCD.

The $U(1)$ model also has a finite integration domain, very similar to the one that we discussed in the toy problem of section 4.2.2. Since the $\cos(z)$ function is periodic with a period of 2π and the measure of the integration domain $[-\pi, +\pi]$ is 2π as well, the application of Lefschetz thimble decomposition is valid here. The flow equation for the $U(1)$ one-link model can be written in the following fashion

$$\begin{aligned}\dot{x} &= -\text{Re } \partial_z S(z) = -\sin(x) \left(\beta \cosh(y) + \frac{\kappa(\cosh(y - \mu) + \kappa \cos(x))}{D(x, y)} \right), \\ \dot{y} &= +\text{Im } \partial_z S(z) = \beta \cos(x) \sinh(y) + \kappa \sinh(y - \mu) \left(\frac{(\cos(x) + \kappa \cosh(y - \mu))}{D(x, y)} \right),\end{aligned}$$

where

$$D(x, y) = (1 + \kappa \cos(x) \cosh(y - \mu))^2 + (\kappa \sin(x) \sinh(y - \mu))^2.$$

κ	Type	Points
$\kappa = 0.5$	Fixed points	$(0.00 + i0.478), (\pm\pi + i3.387), (\pm\pi + i1.171), (\pm\pi - i1.036)$
$\kappa = 0.5$	Singular points	$(\pm\pi + i0.683), (\pm\pi + i3.317)$
$\kappa = 2.0$	Fixed points	$(0.00 + i0.654), (\pm\pi - i0.917), (\pm2.275 + i2.131)$
$\kappa = 2.0$	Singular points	$(\pm2.094 + i2.00)$

Table 6: Fixed and singular points for $\beta = 1, \mu = 2$ and two different values of κ .

We will perform our analysis of the model with fixed values of $\beta = 1, \mu = 2$, and two different values of κ , i.e., $\kappa = 0.5$ and $\kappa = 2.0$. (Fig. 17)

Consider first the case when $\kappa = 0.5$. We can see from Fig. 17a that only the thimble corresponding to the fixed point $z_0 = 0.00 + i0.478$ contributes to the partition function. The anti-thimbles corresponding to all the other fixed points fail to intersect with the original integration contour \mathbb{R} . Only the blue thimble contributes. It is also interesting to note that the thimble for the critical point z_0 and the anti-thimbles for the critical points $z_{1,2} = \pm\pi + i1.171$ overlap with each other completely. This is referred to in literature as *Stoke's phenomenon*, where $\text{Im } S(z_0) = \text{Im } S(z_{1,2})$ and the asymptotic behaviour of the expressions can change abruptly across such values of the parameters. However, we have verified that the thimble structure does **not** change discontinuously as κ is varied around

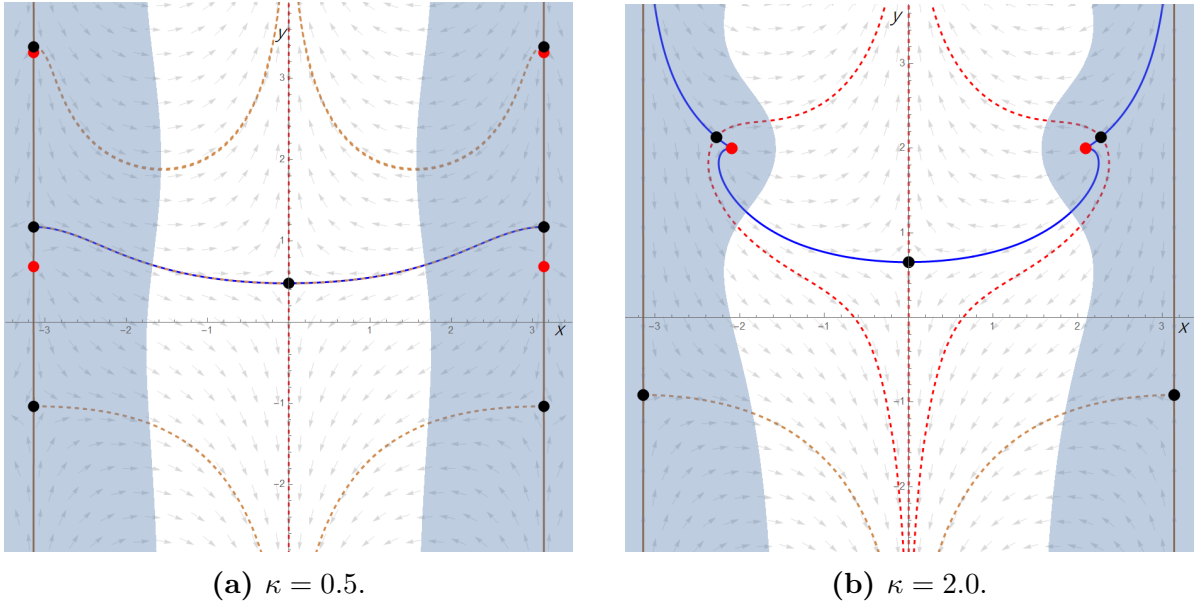


Figure 17: Thimble structure and Lefschetz flow for $U(1)$ model for (a) $\kappa = 0.5$ and (b) $\kappa = 2.0$. As always, the blue lines indicate the thimbles and red lines the anti-thimbles which contribute to the integral. The brown (full) and light-brown (dashed) lines indicate the thimbles and anti-thimbles which do not contribute to the integral. The black dots represent the fixed points, and the red dots indicate the singular points. The thimbles always start and end in the region of convergence $\text{Re } S > 0$ marked with light-blue.

0.5, hence the computation of Z at these parameter values is valid.

For the thimbles at $x = \pm\pi$, we can see that in the regions $x \rightarrow \pm\infty, y \rightarrow \pm\infty$, the action $S \rightarrow \infty$, and the integral is technically convergent there. However, because these lines are exactly parallel to the y -axis, they cannot be a deformation of the original real axis, i.e., they cannot contribute to the integral. It is also interesting to note that the Langevin probability distribution for the same model at $\kappa = 0.5$, as is shown in Fig. 10a, nicely matches with the location of the thimbles in Fig. 17a, hence verifying the agreement between both the algorithms.

Let us now consider the case when $\kappa = 2.0$. For $\kappa > 1$, the thimble structure changes considerably. Note that there are two singular points at $x = \pm\pi$ for $\kappa < 1$. Those singular points merge at $\kappa = 1$ and then move away from $x = \pm\pi$ as $\kappa > 1$. In this process, the central fixed point at $x = \pm\pi$ is absorbed and only one fixed point at $x = \pm\pi$ remains. This can be seen in Fig. 17b. We also see that instead of one contributing thimble, there are now two additional contributing thimbles (related by symmetry) going out to $z = \pm\pi + i\infty$.

We can again compare the thimble structure of the $\kappa = 2.0$ with the Langevin distribution in 10b. As we can see, the heat map of the Langevin distribution is fairly spread out. The contribution from the extra thimbles that appears in Fig. 17b causes the distribution to be fairly spread out across the central and new sideways thimbles, which can explain the similarity with the Langevin case where the distribution is pulled towards the singular points, and causes it to be more spread out than for $\kappa = 0.5$.

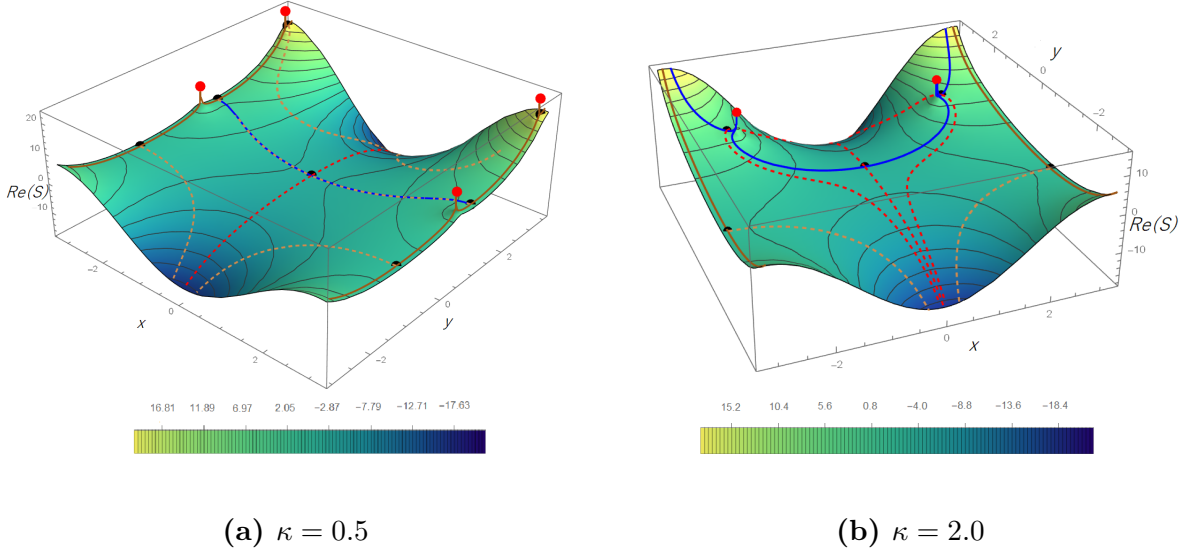


Figure 18: Thimble structures for the $U(1)$ model on the manifold of $\text{Re } S$. As the reader may notice, the $\text{Re } S$ always rises on either side of the saddle point for the thimbles and drops on either side for the anti-thimbles. Hence, the thimbles are the steepest ascent paths for $\text{Re } S$ (consequently, steepest descent path for $\text{Re } \rho = -\text{Re } S$) and vice-versa for anti-thimbles.

Finally, the partition function can be calculated using the thimble decomposition formula

$$Z = \frac{1}{2\pi} \sum_m \langle \mathcal{K}_m, \mathbb{R} \rangle e^{-i \text{Im } S(z)} \int_{\mathcal{J}_m} dz e^{-\text{Re } S(z)}$$

and the observable expectation values can be calculated as

$$\langle O(z) \rangle = \frac{1}{2\pi} \frac{1}{Z} \left[\sum_m \langle \mathcal{K}_m, \mathbb{R} \rangle e^{-i \text{Im } S(z)} \int_{\mathcal{J}_m} dz e^{-\text{Re } S(z)} O(z) \right].$$

Observable	κ	Exact Value	Measured Value
Z	$\kappa = 0.5$	2.32919	$2.30772 - i0.02129$
$\langle U \rangle$	$\kappa = 0.5$	0.36869	$0.36641 - i0.00237$
$\langle U^{-1} \rangle$	$\kappa = 0.5$	1.24872	$1.24553 - i0.00359$
$\langle \cos(z) \rangle$	$\kappa = 0.5$	0.80871	$0.80597 - i0.00298$
$\langle n \rangle$	$\kappa = 0.5$	0.44002	$0.43956 - i0.00059$
Z	$\kappa = 2.0$	5.51854	$5.46343 - i0.05509$
$\langle U \rangle$	$\kappa = 2.0$	0.31522	$0.31318 - i0.00208$
$\langle U^{-1} \rangle$	$\kappa = 2.0$	1.80094	$1.79945 - i0.00126$
$\langle \cos(z) \rangle$	$\kappa = 2.0$	1.05808	$1.05632 - i0.00167$
$\langle n \rangle$	$\kappa = 2.0$	0.74286	$0.74288 + i0.00035$

Table 7: Lefschetz thimbles on $U(1)$ model with $\kappa = 0.5, 2.0$.

The results from the Lefschetz Thimble method simulations for the $U(1)$ model are summarized in 7. The numerical values match nicely with the exact values of the observable expectation values and the partition function Z , even though the model carries some challenges with the singular points appearing in the theory. Therefore, the analysis that we have performed for 0-dimensional theories using Lefschetz Thimble method shows considerable promise. Thus, the method might be a legitimate option for evading the sign problem, if the trend continues for higher dimensional QCD as well.

5 Conclusion: Thimbles and Langevin Dynamics

Over the last few sections, we have described the complex Langevin method and the Lefschetz thimble method comprehensively, with plenty of toy models to verify the applicability of the methods. Therefore, before concluding, it would be good idea to review some similarities and differences between the two methods. [14, 15]

As has been discussed plenty of times by now, both the methods rely on complexification of the field variable ϕ , where the action is described by $S(\phi)$. For Langevin dynamics, the complex evolution equation of the field variable is given as

$$\frac{d\phi}{dt} = - \left. \frac{dS}{d\phi} \right|_{\phi(t)} + \eta(t),$$

where $\eta(t)$ is a real gaussian white noise with variance 2. The Lefschetz flow equation, on the other hand, is of the form

$$\frac{d\phi}{dt} = - \left. \overline{\frac{dS}{d\phi}} \right|_{\phi(t)}.$$

The Lefschetz flow equation differs from the classical complex Langevin equation only by a complex conjugation. While the similarity in the two equations is what leads them to give similar probability distributions, the differences between them cause them to have largely different dynamics.

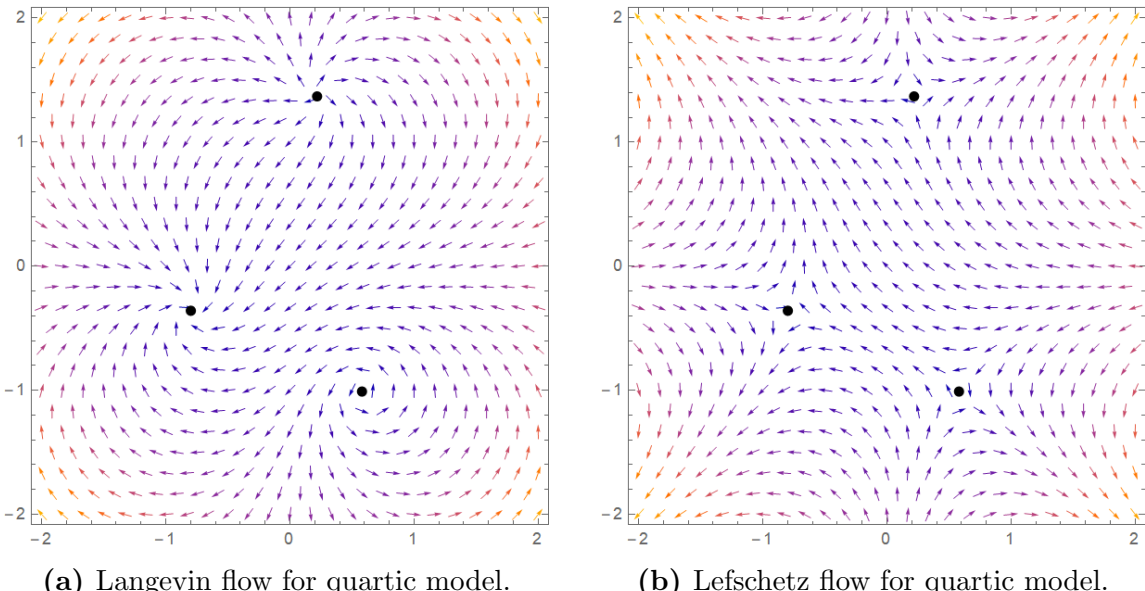


Figure 19

The most obvious difference in the dynamics is the flow around the critical points in both the methods. While the Langevin method only allows the flow around the fixed points to be either attractive or repulsive spiral flows, the Lefschetz flow only admits saddle point-like flow around the fixed points, which is why the method is known as the “Saddle-point” method for 1-D integrals.

This is also related to the stability of the trajectories in both the methods. The thimbles that flow to infinity in the imaginary direction coincide with run-away solutions of the classical CL equations. However, those kind of trajectories can always be avoided in the stochastic process by an appropriate choice of the integration step size in CLM.

Another obvious difference is that complex Langevin dynamics takes place in the whole complexified manifold, in this case the complex plane \mathbb{C} , hence doubling the degrees of freedom of the original problem. The Lefschetz thimbles, on the other hand, are a complex sub-manifold of the complexified domain, but they still have the same dimension of the original domain of integration.

However, because the Lefschetz thimbles are in general curved complex manifolds, we may pick up an additional residual phase due this curvature. But the sign problem due to this residual phase, if present at all, should be much milder than the sign problem in the original integration domain. No such problem arises in complex Langevin dynamics apart from the fact that guaranteeing convergence for CLM is not trivial.

Lastly, thanks to my summer research group, we were able to arrive at the conclusion that although the Lefschetz thimble method allows the calculation of the partition function Z , since it is just a generalised scheme to calculate integrals, the complex Langevin method has no scope to calculate the complex partition function Z . This is because the CL method only allows us to create a sample of points distributed according to some real probability distribution, and calculating a complex measure of such a probability distribution is an impossible task. However, by estimating the volume of the approximated 2-D histogram, we can calculate the norm $|Z|$, and obtain the magnitude of the complex valued partition function.

There are several schemes which aim to unify the complex Langevin and the Lefschetz thimbles method so as utilize the strengths of both the methods [21]. However, we do not approach those at the moment, and leave them as a topic for future exploration. Anyhow, both CLM and LTM are diverse and versatile methods which can serve as an excellent approximation scheme not in just QCD, but even in standard QM integrals, ranging from path integrals to being an alternative to WKB scheme in perturbation methods. Therefore, we hope to see the applications of these methods coming up in various fields of physics in the future which require numerical methods.

References

- [1] Y. Tanizaki, *Study on sign problem via Lefschetz-thimble path integral*. PhD Thesis, The University of Tokyo, December 2015, doi:10.15083/00073296. ([link](#))
- [2] L. Bongiovanni, *Numerical methods for the sign problem in Lattice Field Theory*. arXiv:1603.06458 [hep-lat].
- [3] E. Witten, *Analytic Continuation Of Chern-Simons Theory*, AMS/IP Stud. Adv. Math. **50** (2011), 347-446 arXiv:1001.2933 [hep-th].
- [4] Y. Tanizaki, H. Nishimura, J. J. M. Verbaarschot, *Gradient flows without blow-up for Lefschetz thimbles*, JHEP **10** (2017), 100 doi:10.1007/JHEP10(2017)100 arXiv:1706.03822 [hep-lat].
- [5] S. Bluecher, J. M. Pawłowski, M. Scherzer, M. Schlosser, I. O. Stamatescu, S. Syrkowski, F. P. G. Ziegler. *Reweighting Lefschetz Thimbles*, SciPost Phys. **5** (2018) no.5, 044 doi:10.21468/SciPostPhys.5.5.044 arXiv:1803.08418 [hep-lat].
- [6] G. Parisi and Y. s. Wu, *Perturbation Theory Without Gauge Fixing*, Sci. Sin. **24** (1981), 483 ASITP-80-004. ([link](#))
- [7] K. Okano, L. Schülke, B. Zheng, *Complex Langevin Simulation*, Prog. Theor. Phys. Suppl. **111** (1993), 313-347 doi:10.1143/PTPS.111.313. ([link](#))
- [8] V. Leino, *Master's thesis, The Complex Langevin Method*. University of Helsinki, 2013. ([link](#))
- [9] P. Kumar, *Complex Langevin Dynamics for Complex Actions*, Summer Project Report, 2020. ([link](#))
- [10] R. Kaundinya, *Lefschetz Thimbles for Simple Zero-dimensional Systems*, Summer Project Report, 2020. ([link](#))
- [11] R. Bharathkumar, A. Joseph, *Lefschetz Thimbles and Quantum Phases in Zero-Dimensional Bosonic Models*, Eur. Phys. J. C **80** (2020) no.10, 923 doi:10.1140/epjc/s10052-020-08493-8 arXiv:2001.10486 [hep-th].
- [12] A. Durakovic, E. C. Andre, A. Tranberg, *On Complex Langevin Dynamics and the Evaluation of Observables*, arXiv:1408.3577 [hep-lat].
- [13] G. Aarts, I. O. Stamatescu, *Stochastic quantization at finite chemical potential*, JHEP **09** (2008), 018 doi:10.1088/1126-6708/2008/09/018 arXiv:1308.4811 [hep-lat].
- [14] G. Aarts, L. Bongiovanni, E. Seiler, D. Sexty, *Some remarks on Lefschetz thimbles and complex Langevin dynamics*, JHEP **10** (2014), 159 doi:10.1007/JHEP10(2014)159 arXiv:1407.2090 [hep-lat].

- [15] G. Aarts, *Lefschetz thimbles and stochastic quantisation: Complex actions in the complex plane*, Phys. Rev. D **88** (2013) no.9, 094501 doi:10.1103/PhysRevD.88.094501 arXiv:1308.4811 [hep-lat].
- [16] Gert Aarts, Frank A. James, Erhard Seiler, Ion-Olimpiu Stamatescu, *Adaptive step-size and instabilities in complex Langevin dynamics*, Phys. Lett. B **687** (2010), 154-159 doi:10.1016/j.physletb.2010.03.012 arXiv:0912.0617 [hep-lat].
- [17] Gert Aarts, Erhard Seiler, Ion-Olimpiu Stamatescu, *The Complex Langevin method: When can it be trusted?* Phys. Rev. D **81** (2010), 054508 doi:10.1103/PhysRevD.81.054508 arXiv:0912.3360 [hep-lat].
- [18] G. Aarts, F. A. James, E. Seiler, I.O. Stamatescu. *Complex Langevin dynamics: criteria for correctness*, PoS **LATTICE2011** (2011), 197 doi:10.22323/1.139.0197 arXiv:1110.5749 [hep-lat].
- [19] G. Aarts, P. Giudice, E. Seiler, *Localised distributions and criteria for correctness in complex Langevin dynamics*, Annals Phys. **337** (2013), 238-260 doi:10.1016/j.aop.2013.06.019 arXiv:1306.3075 [hep-lat].
- [20] C. E. Berger, L. Rammelmüller, A. C. Loheac, F. Ehmann, J. Braun, J. E. Drut, *Complex Langevin and other approaches to the sign problem in quantum many-body physics*, Phys. Rept. **892** (2021), 1-54 doi:10.1016/j.physrep.2020.09.002 arXiv:1907.10183 [cond-mat.quant-gas].
- [21] J. Nishimura, S. Shimasaki, *Combining the complex Langevin method and the generalized Lefschetz-thimble method*, JHEP **06** (2017), 023 doi:10.1007/JHEP06(2017)023 arXiv:1703.09409 [hep-lat].
- [22] Sinéad Breen, *Exponentially-improved Asymptotics of Single and Multidimensional Integrals*, PhD Thesis. September 1999. ([link](#))
- [23] David Tong, *Lectures on Kinetic Theory*. ([link](#))
- [24] Steven H. Strogatz, *Nonlinear dynamics and Chaos: With Applications to Physics, Biology, Chemistry, and Engineering*.
- [25] C. M. Bender, S. A. Orszag, *Advanced Mathematical Methods for Scientists and Engineers I: Asymptotic Methods and Perturbation Theory*.
- [26] T. Lancaster and S. J. Blundell, *Quantum Field Theory for the Gifted Amateur*.